



**Environmental
Science**
Processes & Impacts

**Molecular Investigation of the Multi-Phase Photochemistry
of Fe(III)-Citrate in Aqueous Solution**

Journal:	<i>Environmental Science: Processes & Impacts</i>
Manuscript ID	EM-ART-12-2021-000503.R1
Article Type:	Paper

SCHOLARONE™
Manuscripts

1
2
3 **Environmental significance:** Photocatalytic reactions of Fe^{III}-carboxylate complexes in nature play
4 an important role in oxidation of dissolved organic constituents and control bioavailability of iron for
5 development of microbial life. This work presents an experimental study on the molecular
6 photochemistry of an Fe-citrate model system, describing in detail the sequence of its photochemical
7 reactions in the aqueous solution. We characterize water soluble organic and Fe-organic components
8 of the reaction system and reveal formation of insoluble colloidal products containing carbon in
9 reduced oxidation state. The analytical and physical chemistry methods presented in this work can be
10 extended to study photochemistry of other Fe-carboxylate systems.
11
12
13
14
15
16
17
18
19
20
21
22
23
24
25
26
27
28
29
30
31
32
33
34
35
36
37
38
39
40
41
42
43
44
45
46
47
48
49
50
51
52
53
54
55
56
57
58
59
60

1
2
3
4
5
6
7
8
9
10
11
12
13
14
15
16
17
18
19
20
21
22
23
24
25
26
27
28
29
30
31
32
33
34
35
36
37
38
39
40
41
42
43
44
45
46
47
48
49
50
51
52
53
54
55
56
57
58
59
60

Molecular Investigation of the Multi-Phase Photochemistry of Fe(III)-Citrate in Aqueous Solution

Christopher P. West¹, Ana C. Morales¹, Jackson Ryan¹, Maria V. Misovich¹, Anusha P. S. Hettiyadura¹, Felipe Rivera-Adorno¹, Jay M. Tomlin¹, Andrew Darmody², Brittany N. Linn¹, Peng Lin^{1,a}, Alexander Laskin^{1,3*}

¹Department of Chemistry, Purdue University, West Lafayette, IN, USA

²Department of Aeronautics and Aerospace Engineering, Purdue University, West Lafayette, IN

³Department of Earth, Atmospheric & Planetary Sciences, Purdue University, West Lafayette, IN, USA

^aNow at California Air Resource Board (CARB), 1001 I Street, Sacramento, CA, USA

*Correspondence to: alaskin@purdue.edu

Manuscript Submitted to:

Environmental Science: Processes & Impacts

April 8, 2022

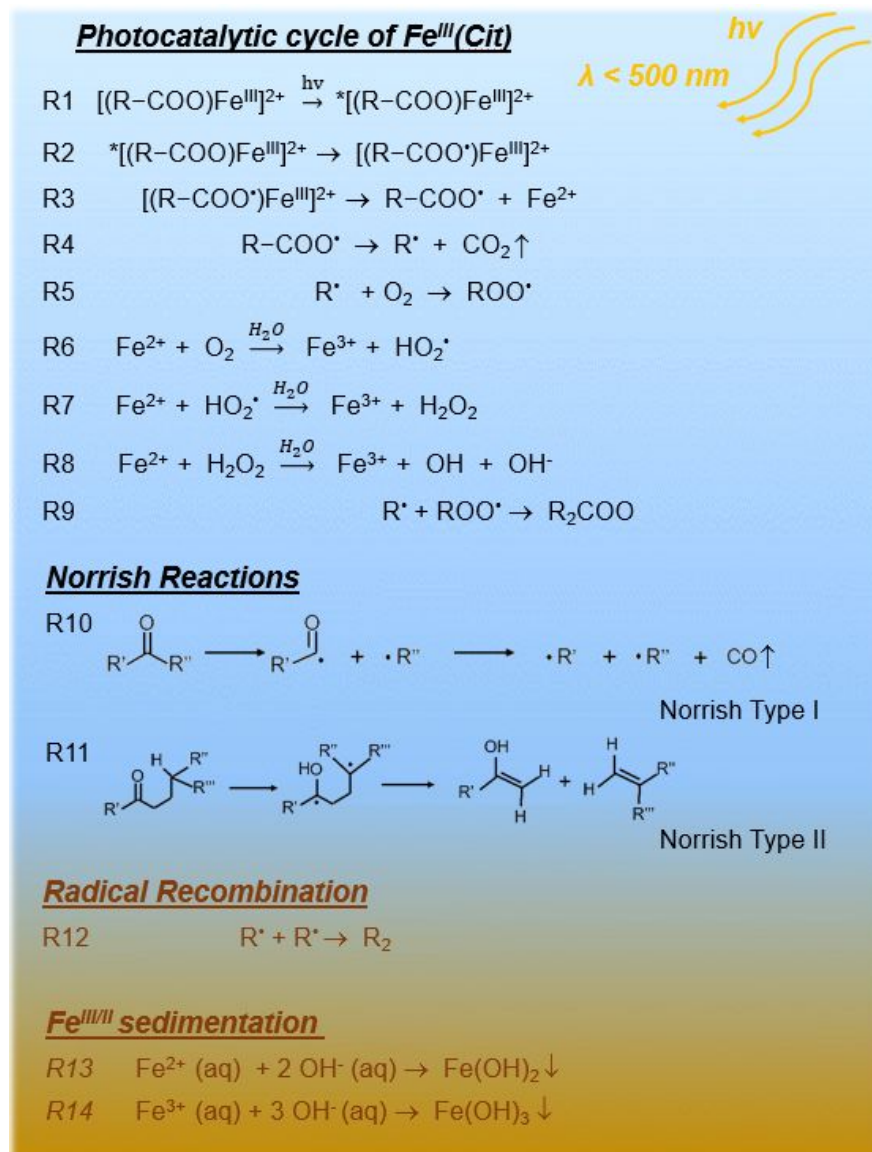
1
2
3 **Abstract:** Iron (Fe) is ubiquitous in nature and found as Fe^{II} or Fe^{III} in minerals or as dissolved
4 ions Fe²⁺ or Fe³⁺ in aqueous systems. The interactions of soluble Fe have important implications
5 on fresh water and marine biogeochemical cycles, which have impacts on global terrestrial and
6 atmospheric environments. Upon dissolution of Fe^{III} into natural aquatic systems, organic
7 carboxylic acids efficiently chelate Fe^{III} to form [Fe^{III}-carboxylate]²⁺ complexes that undergo a
8 wide range of photochemistry-induced radical reactions. The chemical composition and
9 photochemical transformations of these mixtures are largely unknown, making it challenging to
10 estimate their environmental impact. To investigate photochemical processing of Fe^{III}-
11 carboxylates at molecular-level, we conduct comprehensive experimental study employing UV-
12 visible spectroscopy, liquid chromatography coupled to photodiode array and high-resolution mass
13 spectrometry, and oil immersion flow microscopy. In this study, aqueous solutions of Fe^{III}-citrate
14 were photolyzed under 365 nm light in an experimental setup with an apparent quantum yield of
15 (Φ) \sim 0.02, followed by chemical analyses of reacted mixtures withdrawn at increment time
16 intervals of the experiment. The apparent photochemical reaction kinetics of Fe³⁺-citrates (aq)
17 were expressed as two generalized consecutive reactions of *Reactants* (*R*) $\xrightarrow{j_1}$ *Intermediates* (*I*) $\xrightarrow{j_2}$
18 *Products* (*P*) with the experimental rate constants of $j_1 \sim 0.12 \text{ min}^{-1}$ and $j_2 \sim 0.05 \text{ min}^{-1}$,
19 respectively. Molecular characterization results indicate that *R* and *I* consist of both water-soluble
20 organic and Fe-organic species, while *P* compounds are a mixture of water-soluble and colloidal
21 materials. The latter were identified as Fe-carbonaceous colloids formed at long photolysis times.
22 The carbonaceous content of these colloids was identified as unsaturated organic species with low
23 oxygen content and carbon with reduced oxidation state, indicative of their plausible radical
24 recombination mechanism at oxygen-deprived conditions typical for the extensively photolyzed
25 mixtures. Based on the molecular characterization results, we discuss the comprehensive reaction
26 mechanism of Fe^{III}-citrate photochemistry and report on the formation of previously unexplored
27 colloidal reaction products, which may contribute to atmospheric and terrestrial light-absorbing
28 material in aquatic environments.

29
30
31
32
33
34
35
36
37
38
39
40
41
42
43
44
45
46
47
48
49
50
51 **Keywords:** water soluble Fe, Fe-carboxylate complexes, photolysis, reactive oxygen species
52 (ROS), semi-solid colloids, liquid chromatography (LC), UV-visible spectroscopy, high resolution
53 mass spectrometry (HRMS), flow microscopy
54
55
56
57
58
59
60

INTRODUCTION

Iron (Fe) is the most common element on Earth by mass, and found in atmosphere, biosphere, lithosphere, and hydrosphere.^{1,2} A majority of Fe is associated with the solid form of rocks of crustal matter in oxygen-deficient settings,³ whereas soluble and colloidal Fe-containing species are present in oceanic and terrestrial water environments.⁴⁻⁶ Atmospheric Fe is also naturally abundant in wind-blown mineral dust and other components of particulate matter (PM).⁷⁻¹³ The interactions, transport, and environmental fate of elemental Fe are vital in the Fe biogeochemical cycle and necessary to sustain life and facilitate important environmental processes.^{14,15} The soluble fractions of Fe from Fe-bearing materials¹⁶⁻¹⁸ are mobilized in aquatic environments as a result of various chemical processes such as photolysis and reactions with inorganic acids. Upon dissolution of Fe into aquatic aerobic systems (pH 4 – 8), available organic carboxylic acid components of dissolved organic matter (DOM) efficiently chelate Fe³⁺ ions to form photocatalytically active [Fe^{III}-carboxylate]²⁺ complexes that promote radical reactions in the aquatic phase. Upon excitation by UV-visible light, the photochemically initiated radical reactions modify the composition of DOM with subsequent effects on optical and physical properties of the environmental aquatic systems.¹⁹

Molecular-level characterization of reactive components in the Fe-carboxylate photochemical systems is still largely lacking and reported results remain ambiguous. Previous studies utilized optical spectroscopy,²⁰⁻²⁴ electrochemistry,²¹ and liquid chromatography with optical detection²⁵ to infer reaction mechanisms and system properties solely from measurements of the bulk solution, but not for the molecular-specific components. However, unravelling the molecular-specific processes leading to the conversion of solid Fe^{III} to soluble Fe³⁺, Fe³⁺ complexation with carboxylic acids, and the environmental reactions of [Fe^{III}-carboxylate]²⁺ complexes are still needed for quantitative predictions of Fe^{III}-carboxylate photochemistry in aquatic systems.



Scheme 1. Reaction sequence of the photo-catalytic redox cycle of Fe^{III}-citrate complex in aquatic environment. R in reactions R1-R5 and R9 corresponds to -(CH₂CO₂H)₂COH, ‘R, “R, and ““R symbols indicate various parts of organic molecules. Mononuclear monocitrate (or 1:1 complex, [(R-COO)Fe^{III}]²⁺) is shown here as a representative complex in the reaction scheme. Herein, legends of Fe²⁺ and Fe³⁺ refer to dissolved ions, whereas legends of Fe^{III} and Fe^{II} indicate complexation with ligands.

Photoreactive Fe^{III}-carboxylate complexes absorb light at wavelengths below 500 nm, which catalyzes ligand to metal charge transfer (LMCT) reactions, resulting in the reduction of Fe^{III} to Fe^{II} and oxidation of the carboxylate ligands, a process that represents an important sink of organic acids in marine, terrestrial, and atmospheric water.^{22,26-31} Scheme 1 summarizes these and other

1
2
3 relevant aquatic reactions. The LMCT process occurs as a result of an electron transfer from the
4 innermost sp^3 orbital of the carboxylate ligand to the metal center, forming $[Fe^{III}-COO-R]^{2+*}$ -
5 excited state and the $[Fe^{III}-COO^{\bullet}-R]^{2+}$ radical complex, as shown in R1-R2.³² The equivalent
6 lifetime of the intermediate radical complex, determined in previous studies,^{24,33-35} was found to
7 be on the order of a few milliseconds, after which it decomposes into Fe^{2+} and $R-COO^{\bullet}$ as shown
8 in R3. Further reactions of Fe^{2+} and $R-COO^{\bullet}$ lead to loss of CO_2 as shown in R4, forming alkyl
9 radicals (R^{\bullet}).³⁶⁻³⁸ Organic peroxy radicals (RO_2^{\bullet}) are later formed in the reaction with oxygen
10 (O_2) as shown in R5.³⁹ Additional reactions of Fe^{2+} ions with dissolved O_2 lead to the formation of
11 reactive oxygen species (ROS)⁴⁰⁻⁴² such as HO_2^{\bullet} , hydrogen peroxide (H_2O_2), and hydroxyl radicals
12 (OH^{\bullet})⁴³⁻⁴⁵ while cycling Fe^{2+} back to Fe^{3+} through the Fenton reaction,⁴⁶ as shown in R6-8. The
13 ROS species react further with a variety of organic and inorganic compounds in aqueous
14 solution.⁴⁷⁻⁵⁰ Subsequently, organic peroxy radicals (ROO^{\bullet}) in solution may decompose into
15 smaller organic acid fragments such as oxygenated volatile organic compounds (OVOC), or
16 undergo radical recombination reactions as shown in R9, and R12 resulting in production of larger
17 oligomeric species.

18
19
20
21
22
23
24
25
26
27
28
29
30
31 Radical species with carbonyl groups formed after decarboxylation, may undergo Norrish type I
32 and II reactions as shown in R10-11,⁵¹⁻⁵⁴ triggering radical chain reactions with O_2 and various
33 organic compounds. Norrish reactions produce carbon monoxide (CO) and carbon-centered
34 radicals (CCRs), such as methyl ($^{\bullet}CH_3$), methyl ketones ($O=^{\bullet}C-CH_3$), and
35 triphenylmethyl ($^{\bullet}C(C_6H_5)_3$), among other radicals.⁵⁵ As a result, the dissolved oxygen is
36 effectively consumed, while the CO_2 and CO products are degassed, resulting in oxygen-deficient
37 conditions after prolonged photolysis. As shown in R12, radical recombination forms compounds
38 with lower oxygen content and carbon in reduced oxidation state. These products have much lower
39 solubility than oxygenated organic carbon and therefore may contribute to the buildup of insoluble
40 photomineralization products.^{56,57} In addition to the reduced carbon colloids, precipitation of
41 insoluble iron hydroxides,¹⁹ $Fe(OH)_2$ and $Fe(OH)_3$, can take place as shown in R12-13,^{58,59} which
42 further contributes to the formation and growth of colloid particles. The insoluble colloids of
43 mixed $Fe(OH)_3$ /carbonaceous composition exhibit substantially larger light extinction properties
44 than the water-soluble components in the same mixtures.⁶⁰

1
2
3 Multiphase aquatic photochemistry of Fe^{III}-citrate has been studied^{20,25,41,55,61,62} as a laboratory
4 proxy for the environmental Fe^{III}-carboxylate systems. To date, the production and detection of
5 gas-phase OVOC upon photolysis of Fe^{III}-secondary organic aerosol proxies containing carboxylic
6 acids in flow reactors⁶³ have been investigated. Other studies reported changes in the
7 microphysical properties, chemical composition, and ROS capacity of viscous Fe-citrate particles
8 levitated in electrodynamic balance and probed by spectromicroscopy after exposure to UV
9 light.^{41,55} These studies^{41,55} demonstrated significant photochemical degradation after 24 hours of
10 irradiation, resulting in ~ 80% mass loss of particles due to degassing of CO₂ and OVOC, and slow
11 uptake/molecular diffusion of O₂ in the particle phase, consistent with reactions R1-8 of Scheme
12 1. The combination of these studies provides surface and physical property characterization
13 results. However, molecular-level composition, optical properties, and extent of the photochemical
14 reactions occurring in the condensed phase are still insufficiently investigated. This knowledge
15 gap precludes quantitative predictions of the photocatalytic processing for Fe-carboxylate systems
16 and their consequences on environmental systems.
17
18

19
20
21
22
23
24
25
26
27
28
29 In this work, the chemical composition and optical properties of aqueous Fe^{III}-citrate
30 photocatalytic components were investigated using high-performance liquid chromatography
31 coupled to a photodiode array and high-resolution mass spectrometry (HPLC-PDA-HRMS)
32 detectors,⁶⁴⁻⁷¹ and were further evaluated with direct infusion (DI) HRMS chemical analysis.^{66,70,72}
33 Colloidal products produced during photolysis reactions were imaged with *in situ* oil immersion
34 flow microscopy. Multi-modal datasets from these complementary techniques provide a unique
35 experimental description of various stages of Fe^{III}-citrate photochemistry, elucidate individual
36 components of this reacting system, determine mechanistic insights, and quantify environmental
37 parameters affecting the Fe^{III}-carboxylate photochemistry.
38
39
40
41
42
43
44
45
46

47 **EXPERIMENTAL METHODS**

48
49
50 **Sample Preparation** 10mM stock solutions of ferric citrate (C₆H₅O₇Fe, 16.5 – 18.5 % Fe basis,
51 BioReagent, CAS: 3522-50-7; Sigma Aldrich Inc.) and of citric acid (C₆H₈O₇·H₂O; 99% purity,
52 Mallinckrodt Inc.) analytical blank for HPLC analysis were prepared in 100mL borosilicate
53 volumetric flasks using 18.1 MΩ cm⁻¹ Milli-Q ultrapure water. The stock solutions were wrapped
54
55
56
57
58
59
60

1
2
3 in aluminum foil (Fisher Inc.) and stored in a refrigerator at ~ 5 °C. The ferric citrate stock solution
4 were further diluted to $\sim 9.0 \times 10^{-5}$ M (90 μ M) in the ultrapure water and were set to equilibrate
5 for ~ 2 -24 h in the dark prior to chemical characterization, as recommended in the literature.^{73,74}
6
7
8

9
10 **Photochemical Experiments and Optical Spectroscopy measurements.** A custom-built
11 photolysis reactor setup employing a constant wavelength light emitting diode (LED) that emits
12 blue light at $\sim 365 \pm 9$ nm (Model: M365LP1; Thor Labs Inc.) was placed ~ 20 cm above the
13 sample compartment (qpod2e, Quantum Northwest Inc.). The sample was placed in a 10 mm
14 quartz cuvette (Vernier Inc.). The mounted UV- LED optics and adjusted collimator lens in these
15 experiments resulted in an illuminated cross-sectional area of 0.78 ± 0.05 cm². All experiments
16 were conducted at room temperature (~ 24 -26 °C), and temperature was monitored throughout the
17 reaction. Additional details of the experimental methods and instrumentation parameters are
18 described in Figure S1 (Appendix A of the SI file). UV-Visible absorption spectra of the
19 photolyzed solutions were acquired using a USB 2000 UV-Vis-NIR (Ocean Optics Inc.) fiber
20 optic spectrophotometer. The samples were analyzed over the 200 – 900 nm wavelength range
21 employing 20 ms integration time, 6 scans to average, and boxcar width of 4.
22
23
24
25
26
27
28
29
30
31

32 The spectral flux of the LED radiation (F_{LED}) experienced by the samples was experimentally
33 determined by the chemical actinometry method using a 1 mM solution of potassium ferrioxalate
34 ($K_3[Fe(C_2O_4)_3]$; Sigma-Aldrich) in 0.05M sulfuric acid (Honeywell Inc.), described by Lehóczyki
35 et al., 2013.⁷⁵ The decrease in absorption of ferrioxalate ($\epsilon_{Fe-Ox} \sim 312 \pm 2$ L mol⁻¹ cm⁻¹ at 390 nm)⁷⁵
36 as a function of irradiation time was measured and converted to the $F_{LED} \sim 3.85 \times 10^{15}$ photons
37 cm⁻² s⁻¹ at 365 nm, with a quantum yield, $\Phi \sim 1.26$. Description and results of flux calculations
38 is provided in Appendix B and Figure S2 of the SI file.
39
40
41
42
43
44
45

46 **Quantitation of Dissolved Fe²⁺** Quantification of Fe²⁺ concentrations in irradiated solutions
47 employed colorimetric tests with 1,10-phenanthroline (C₁₂H₈N₂; $\geq 99\%$ purity, Sigma-Aldrich
48 Inc.), whereby dissolved Fe²⁺ ions and 1,10-phenanthroline form a red-orange complex that
49 absorbs visible light at ~ 510 nm.^{76,77} For analysis, 0.5 mL of analyte sampled at 0, 5, 20, 40, 80,
50 and 120 min irradiation time were mixed with 1.5 mL of 5mM 1,10-phenanthroline and filled to
51 3mL with 1mL of 18.1 M Ω cm⁻¹ Milli-Q ultrapure water. Quantitative [Fe²⁺] measurements were
52
53
54
55
56
57
58
59
60

1
2
3 performed in triplicate to establish reproducibility. For calibration, chemical standards of Fe^{II}
4 perchlorate hydrate (Fe(ClO₄)₂·H₂O; 98% purity, Sigma Aldrich Inc.), ranging from 1-90 μM
5 concentrations, were mixed with 5 mM 1,10- phenanthroline, and their respective absorbances
6 were measured and recorded via a seven-point calibration curve (Figure S3 in SI file). The limit
7 of detection (LOD) and molar absorptivity ($\epsilon_{510\text{nm}}$) obtained from calibration measurements in this
8 study are ~ 2.3 μM and ~ 7400 L mol⁻¹ cm⁻¹, respectively.
9
10
11
12
13
14

Chemical Characterization 300 uL aliquots of the initial (non-photolyzed) and irradiated
15 mixtures were withdrawn from the cuvette containing 3 mL of experimental solutions at 0, 5, 40,
16 80, and 120 min. Components of the Fe-citrate mixtures were characterized using a VanquishTM
17 high performance liquid chromatography (HPLC) system equipped with an autosampler, a
18 photodiode array (PDA) detector, and a Q ExactiveTM HF-X Orbitrap mass spectrometer
19 interfaced with an IonMAX source which housed a heated electrospray ionization (HESI) probe
20 operated in negative ion mode (all from Thermo Scientific Inc.). Chemical constituents were
21 separated on a zwitterionic hydrophilic interaction liquid chromatography (ZIC-HILIC) column
22 (SynchronisTM, 2 mm × 150 mm, 5 μm particles, 100 Å pore size, Thermo Inc.). ZIC-HILIC
23 column can retain ionic and highly polar, hydrophilic compounds, through liquid-liquid
24 partitioning, electrostatic interactions, and hydrogen bonding,⁷⁸ which cannot be separated on
25 conventional reversed-phase LC columns.⁷⁹ The incorporation of a zwitterionic HILIC stationary
26 phase is particularly applicable for retention of highly polar species such as charged metal-organic
27 complexes (i.e. Fe-citrate, Fe-malate, and Fe-siderophores).⁸⁰⁻⁸⁵ A multistep gradient elution was
28 performed at a flow rate of 0.2 mL min⁻¹ using a binary mobile phase-buffer system: (A) LC/MS-
29 grade water (OptimaTM, Sigma Aldrich Inc.) with 10 mM ammonium acetate buffer (v/v) and (B)
30 LC/MS-grade methanol (OptimaTM, Sigma Aldrich Inc.) with 10 mM ammonium acetate buffer
31 (Sigma Aldrich Inc.). The buffer pH for all LC experiments was held within 5.2 - 6.8 to preserve
32 the metal-ligand equilibria.⁸⁴ Elution proceeded as follows: 0–3 min held at 95% B, 3–7 min linear
33 gradient to 20% B, 7–15 min held at 20% B, 15-19 min linear gradient to 95% B, and re-
34 equilibration period at 19-57 min held at 95% B to prepare for the next injection in the sequence.
35 The autosampler compartment temperature where sample vials were stored was held at 15°C. The
36 column temperature was held at 35°C and an injection volume of 15 μL (~258 ng of injected
37 organic analyte) was used. No additional sample preparation was performed, and samples were
38
39
40
41
42
43
44
45
46
47
48
49
50
51
52
53
54
55
56
57
58
59
60

1
2
3 directly withdrawn and analyzed from the irradiated solutions. The UV–visible absorption spectra
4 of LC-separated components were measured using the PDA detector equipped with a deuterium
5 light-source and 1.0 cm fused-silica LightPipe™ flow cell, with a wavelength range of 200–680
6 nm (3D Field spectra), a scan rate of 20 Hz, and $\lambda \pm 4$ nm spectral resolution. The following
7 conditions were used for the HESI source operation in the HPLC experiments: 40 °C probe heater
8 temperature, 100 °C capillary temperature, 30 units of sheath gas flow, 10 units of auxiliary gas
9 flow, 0 units of sweep gas flow, 3.5 kV spray potential, and a funnel RF level of 30. A method
10 blank was used for all LC-PDA-HRMS experiments, corresponding to 90 μ M citric acid standard.
11 Analyzed samples were ionized in the negative ionization mode and HPLC-PDA-ESI(-)/HRMS
12 datasets were acquired using Xcalibur software (Thermo Inc.). The HRMS was operated at $m/\Delta m$
13 240,000 resolving power at 200 m/z , at a scan rate of 1.5 Hz in the full MS scan mode of 100 –
14 1300 m/z range. Custom mass calibration was performed using commercial calibration solutions
15 (Thermo Scientific, PI-88324) ionized in the negative ESI mode.
16
17
18
19
20
21
22
23
24
25
26

27 Additionally, two sets of HRMS experiments were performed by (1) directly infusing (DI-HRMS)
28 Fe^{III} -citrate solutions photolyzed at 0, 5, 40, 80, and 120 minutes (Exp. 1) in the negative mode to
29 screen for overall water soluble Fe^{III} -citrate components and their photochemical products, and
30 (Exp. 2) to specifically probe components of the unreacted and 120 min irradiated sample for
31 colloidal/carbonaceous products dissolved in 1 mL of a mixture of organic solvents (2:2:2:1 v/v%,
32 acetonitrile (ACN)/dichloromethane (DCM)/ hexanes/ toluene), the ‘*org-mix*’ hereafter, in the
33 positive ion mode. After this step, colloidal mixture underwent dissolution and intentional
34 disruption assisted by ultrasonication for ~ 40 min, followed by filtering using 0.45 μ m PTFE
35 syringe filter cartridges (Thermo Inc.), and solvent evaporation on the TurboVap (Biotage Inc.) at
36 1.5 L min^{-1} flowrate to ~ 1 mL level of remaining water solvent. 20% methanol was added before
37 DI-HRMS as recommended in the literature.^{73,74} DI-HRMS experiments were conducted using
38 similar MS tune conditions described above at 5 μ L min^{-1} injection flow rate for the water-soluble
39 fraction and slightly modified tune parameters for analysis of the colloid components dissolved in
40 the *org-mix*. For the analysis of colloid components dissolved in *org-mix*, the sheath, auxiliary gas
41 flow, funnel RF-level, capillary, and source heater temperature were adjusted to 30, 10 arbitrary
42 units, 80, 250 °C and 100 °C, respectively to allow for efficient droplet desolvation, ionization and
43 detection of larger molecular weight species. In Exp. 1 and Exp. 2 mass spectra were acquired in
44
45
46
47
48
49
50
51
52
53
54
55
56
57
58
59
60

1
2
3 negative and positive modes, respectively. Targeted MS² experiments were performed for
4 structural characterization of selected components of the Fe-citrate mixtures in the negative mode.
5 Additional details of DI-HRMS and targeted MS² experiments are described in Appendix C of the
6 SI file.
7
8
9

10
11 **Data Processing & Analysis.** Raw Xcalibur data files were background-subtracted prior to data
12 processing and analysis to remove any signal attributed to the method blank. The HPLC-
13 ESI/HRMS datasets were batch-processed with customized java script in the open-source
14 software, MZmine 2 (v. 2.51, <http://mzmine.github.io/>), to perform data preprocessing,
15 chromatogram construction, peak deconvolution, peak smoothing, peak alignment, peak
16 annotation, and analyte identification with the CAMERA R-package (Bioconductor R-
17 repository).^{86,87} The ADAP chromatogram builder⁸⁸ was used to reconstruct extracted ion
18 chromatograms (EIC) and obtain the output chromatographic feature list, using a minimum peak
19 height of 10³, LC peak duration of 0.6 min, and mass tolerance of 0.001 m/z. The combined
20 software algorithm identifies the analyte species, assuming the annotated ions in the range 100 –
21 1300 m/z were formed by the loss of a proton in the ESI(–) mode. The detected peaks identified
22 by MZmine 2 were cross evaluated using the Xcalibur software (Thermo Scientific Inc.), thus
23 eliminating erroneous formula assignments occasionally made by the algorithm. In addition, the
24 overall screenings of the Fe-containing peaks detected in the bulk samples were performed in DI-
25 ESI(–/+)/HRMS experiments. Obtained data sets were extracted with the DeconTools
26 AutoProcessor software developed at the Pacific Northwest National Laboratory (v. 1.0;
27 <http://omics.pnl.gov/software/>)⁸⁹ and processed using custom Excel macros (Microsoft Inc.)
28 developed for mass alignment, background subtraction, and ¹³C isotope filtering. Formula
29 assignments were assisted with grouping of the homologous species assigned based on first-order
30 (CH₂) and second-order (CH₂, H₂) Kendrick mass defects, followed by the group-representative
31 formula assignments⁹⁰ using the MIDAS molecular formula calculator (v 1.1;
32 <http://nationalmaglab.org/user-facilities/icr/icr-software>). Isotope distributions of Fe-containing
33 peaks were compared with results obtained from mass spectral isotope distribution simulator
34 software, IsoPro (v. 3.0; <https://sites.google.com/site/isoproms/>), as well as isotope peak scanner
35 function in MZmine 2 to search for m/z and intensity distribution of a calculated isotope pattern
36 within the feature list. The following constraints were applied for all formula assignments: C₁₋₆₀,
37
38
39
40
41
42
43
44
45
46
47
48
49
50
51
52
53
54
55
56
57
58
59
60

H₁₋₁₀₀, O₀₋₂₂, Fe₀₋₅, charge ≤ 2, and mass tolerance of ± 3 ppm. MS peaks with a signal to noise (S/N) ratio ≥ 5 were only considered for this analysis. Double-bond equivalent (DBE) values of the neutral assigned species were calculated using the following equation⁹¹:

$$DBE = C - H/2 + N/2 + 1. \quad (1)$$

Throughout the manuscript, all molecular formulas discussed in the text below correspond to neutral molecules in case of C_xH_yO_z composition and to ions in case Fe-containing organic compounds, superscripted by their corresponding charges.

Calculation of Mass Absorption Coefficient ($MAC_{\lambda,OM}$)

Optical Measurements of Bulk Solutions. The absorption spectra presented in this work are in the units of wavelength-dependent mass absorption coefficient ($MAC(\lambda)_{bulk}$ eq. 2),⁹² which is calculated from log base-10 absorbance ($A_{10}^{solution}$) of the aqueous solution with organic mass (OM) concentration (C_{mass} , g m⁻³), and optical path length ($b = 0.01$ m).

$$MAC(\lambda)_{bulk}(\text{m}^2 \text{g}^{-1}) = \frac{A_{10}^{solution}(\lambda) \times \ln(10)}{b \times C_{mass}} \quad (2)$$

Whereas C_{mass} is calculated as mass concentration of the organic component (i.e., citrate, C₆H₅O₇³⁻). Therefore, C_{mass} in the case of 90 μM Fe-citrate (C₆H₅FeO₇) is ~ 17.02 g m⁻³. The calculation assumes that total OM value does not change in the reacted Fe-citrate mixtures. This assumption, however, underestimates $MAC(\lambda)_{bulk}$ values as decarboxylation reactions produce CO₂ and small oxygenated VOC products, which can volatilize from the solution, therefore reducing OM concentration in the reacted solutions. The open headspace in the experimental setup leads to evaporation and degassing of VOC products from photoreacted solutions. Thus, the computed $MAC(\lambda)_{bulk}$ values reported here should be viewed as the lower estimates. The wavelength dependence of $MAC(\lambda)_{bulk}$ expressed through absorption Ångström exponent (AAE) was assumed using the following formula:

$$MAC(\lambda)_{bulk} = k \times \lambda^{-AAE} \quad (3)$$

AAE values were derived by computing the slope of the linear dependence of $MAC(\lambda)_{bulk}$ versus wavelength plotted on a ln-ln scale, while k is the imaginary part of the refractive index.⁹³ For the analytes of this study, we calculate AAE over 250-450 nm spectral range.

Photodiode Array (PDA) Optical Measurements of Solution Components. The $MAC(\lambda)^{PDA}$ values derived from integrated UV-vis records obtained in LC-PDA measurements and corresponding to the total light absorption in each of the aliquot samples were computed using eq. 4.^{94,95}

$$MAC(\lambda)_{\Sigma}^{PDA} (\text{m}^2 \text{g}^{-1}) = \frac{A(\lambda)_{\Sigma}^{PDA} (\mu\text{AU}) \times \Delta t \times F \times \ln(10)}{b (\text{cm}) \times m_{inj} \times 10} \quad (4)$$

In this analytical expression, $A(\lambda)_{\Sigma}^{PDA}$ is the optical absorbance from PDA detector recorded at wavelength λ over the period of LC separation ($\Sigma = 0 - 12$ min), including the unretained fraction eluting at 0 - 3 min. Δt is the elution time range (12 min); F is the LC flow rate (0.2 mL min^{-1}); b is the optical pathlength of the PDA flow cell (1 cm), and m_{inj} is the injected mass (258 ng) of OM analyte. The coefficient 10 accounts for the combined conversion of μAU into AU, cm^3 into m^3 , cm into m, and ng into g.^{94,95}

The relative fractional contributions of $MAC(\lambda)_i^{PDA}$ attributable to each of the individual LC-separated features (i) in the analyzed samples were computed using equation 5.

$$MAC(\lambda)_i^{PDA} = MAC(\lambda)_{\Sigma}^{PDA} \times \left(\frac{A(\lambda)_i^{PDA} \times \Delta t_i}{A(\lambda)_{\Sigma}^{PDA} \times \Delta t_{\Sigma}} \right) \quad (5)$$

where $A(\lambda)_i^{PDA}$ (μAU) is the averaged UV-visible absorbance of the individual feature i and Δt_i (min) is its time duration. All UV-visible absorption data presented here were processed and exported using custom MATLAB (R2018a, MathWorks Inc., USA) scripts developed in our group. In our study, we report on the molecular composition of the Fe-Citrate reacting mixture and specify the individual $MAC(\lambda)_i^{PDA}$ contributions as a function of reaction time. From there, we

1
2
3 incorporate a ‘bottom up’ approach to interpret optical transformations of the bulk Fe-citrate
4 material in terms of a practical concept of simplified sequential reactions where first-order reaction
5 kinetics are quantified based on computed $MAC(\lambda)_{bulk}$ values.
6
7
8
9

10 ***In Situ* Flow Microscopy Detection of Colloids.** 300 μL of the unreacted, 5 min, 40 min, 80 min,
11 and 120 min irradiated solutions sampled from same cuvette were analyzed *in situ* using a
12 FlowCam[®] Nano instrument (Yokogawa Fluid Imaging Technologies Inc.) operated with the
13 VisualSpreadsheet 5.6.26 software (Fluid Imaging Technologies). The FlowCam[®] Nano
14 instrument uses oil immersion flow microscopy^{96,97} to focus and image particles as they pass
15 through a flow cell. Prior to imaging experiments, the instrument was autofocused with NIST
16 Traceable Polymer Microspheres standard (Lot No: 247697) with known diameter (D_p) of 0.702
17 ± 0.006 μm . The background intensity in all experiments were measured within the 173-178 A.U.
18 range. The instrument parameters are as follows: x40 objective lens, 0.1 μm distance to nearest
19 neighbor, threshold dark/light 18/18, 1 close hole (iterations), 60 μm flow cell depth, 500 μm flow
20 cell width, 0.3 mL sample volume, 0.025 mL min^{-1} sampling flow rate, auto image rate of 137
21 frames s^{-1} , sample run time 12.00 min, particle size range 0.3 – 60 μm when operated in relative
22 count mode. Particle number concentrations were determined using count calibrated mode with
23 the instrument default settings of 0.1 μm distance to nearest neighbor, threshold dark/light 20/20,
24 1 close hole (iterations), 60 μm flow cell depth, 500 μm flow cell width, 0.3 mL sample volume,
25 0.025 mL min^{-1} sampling flow rate, auto image rate of 137 frames s^{-1} , sample run time 12.00 min,
26 and a particle size range 0.3 – 60 μm . After each measurement, the microfluidic system was rinsed
27 with 0.20 μm filtered Windex[®] or 0.1% Liquinox surfactant soap in water (Optima[™], Sigma
28 Aldrich Inc.) followed with a rinse of pure water. Diameters reported from this measurement are
29 equivalent size diameter.
30
31
32
33
34
35
36
37
38
39
40
41
42
43
44
45

46 RESULTS AND DISCUSSION

47
48
49 **Photolysis of the Fe^{III}-Citrate aqueous system.** Figure 1a shows the $MAC(\lambda)_{bulk}$ absorption
50 spectra of the Fe^{III} citrate system measured at selected time intervals during the photolysis
51 experiment. Figure 1b further illustrates evolution of the same $MAC(\lambda)_{bulk}$ spectra but shown as a
52 continuing progression recorded at 5 s intervals using transient optical spectroscopy. The plots
53 show very rapid decrease of the MAC values over the first ~ 5 min of the irradiation, followed by
54
55
56
57
58
59
60

gradual increase over next ~100 min of the experiment. From the beginning of the reaction and during the initial decrease, $MAC(\lambda)_{bulk}$ spectra show a significant drop in their AAE values (from 6.86 to 4.21) but remain featureless. In contrast, over the follow-up increase period, $MAC(\lambda)_{bulk}$ spectra consistently show buildup of an absorption feature at 256 nm and AAE values of the spectra show only moderate change (from 4.21 to 3.62). Figure 1c shows a time-resolved record of MAC_{256nm} values over the entire irradiation time, indicating a reaction trend consistent with the formal kinetics of two first-order consecutive reactions of *Reactants* (R) $\xrightarrow{j_1}$ *Intermediates* (I) $\xrightarrow{j_2}$ *Products* (P). Figure 1c shows kinetic modeling results using this apparent first-order kinetic scheme, featuring relative concentration profiles of R , I , and P components. Details of the kinetic model are described in Appendix D of the SI file. The pH of the initial ferric citrate solution was measured to be 6.7 and changes slightly to 6.52 in the 120 min photoreacted sample. Therefore all photolysis reactions were reproduced within the narrow pH range of this study.

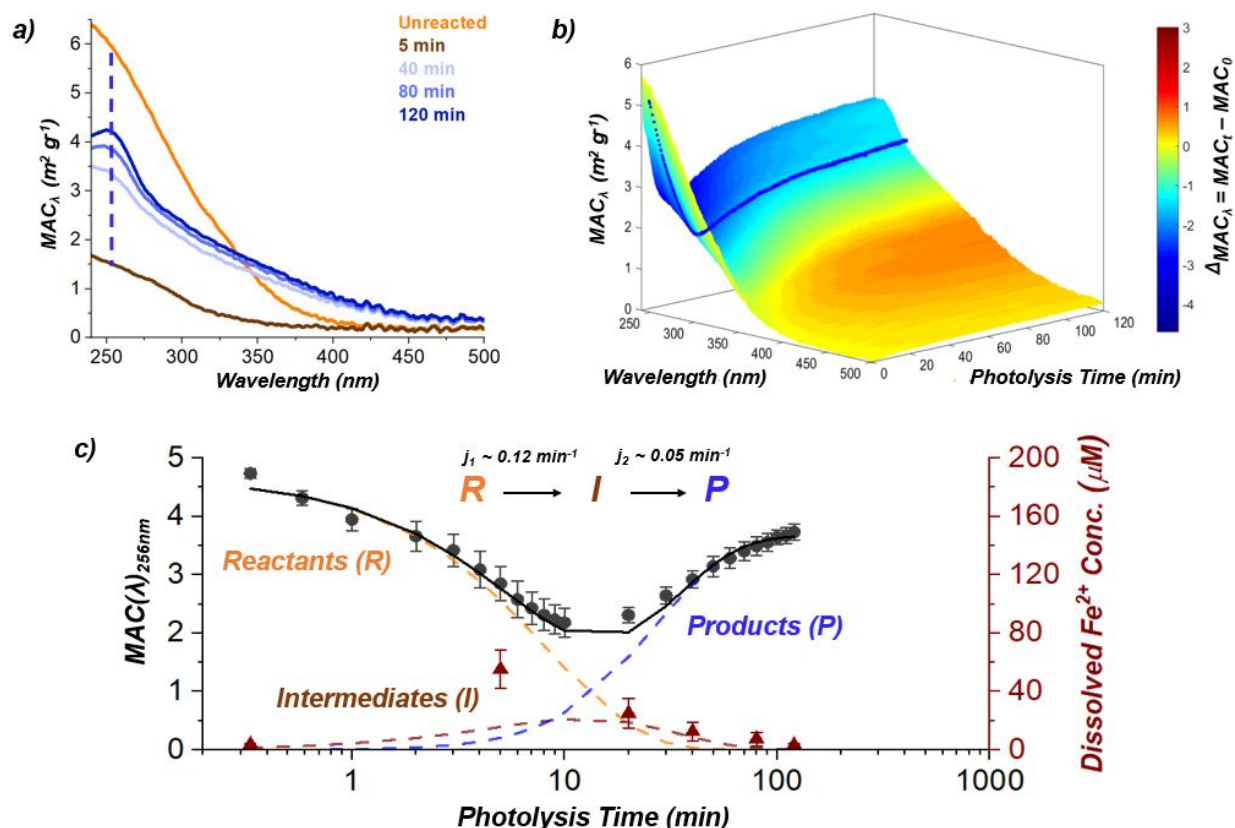


Figure 1. a) $MAC(\lambda)$ spectra of 90 μM Fe^{III}-citrate (1:1 M:L) solution undergoing photochemical transformations recorded at $t = 0, 5, 40, 80, 120$ min of irradiation time. Dashed line indicates absorption at 256 nm b) 3D $MAC(\lambda)$ plot illustrating the same transformations recorded at high time resolution (5s) in

1
2
3 a separate experiment. The x, y, and z-axis represent the absorbing wavelength (nm), MAC_{λ} , and photolysis
4 time (min), respectively. Colormap is scaled by the difference in MAC units ($\Delta MAC = MAC_t - MAC_0$). 2D
5 contour line indicating transient absorption at 256 nm. c) Single-wavelength $MAC_{256\text{nm}}$ experimental data
6 of the Fe^{III} -citrate photolytic time-resolved transformations (black circles, error bars represent standard
7 deviation of 3 replicated measurements). The reaction extent is modeled (dashed lines) using Apparent First
8 Order Kinetics for a formal mechanism of two consecutive irreversible reactions: $Reactants (R) \rightarrow$
9 $Intermediates (I) \rightarrow Products (P)$. Right Y axis of figure 1c shows the overall concentrations of Fe^{2+} ions
10 (brown triangles) measured in the solutions at 0, 5, 20, 40, 80, 120 min of irradiation time.

11
12
13
14
15
16
17 The $MAC(\lambda)_{bulk}$ spectrum of the original Fe^{III} -citrate solution (Fig 1a, orange trace) exhibits
18 characteristic tailing that extends to the visible region of the spectrum. These absorption
19 characteristics are very consistent with previous literature reports,^{21,22,61,98,99} and are similar to
20 optical characteristics exhibited by other Fe^{III} – carboxylate complexes.^{34,100–102} Spectral
21 characteristics of Fe^{II} -ligand species presented here and in the later text may be attributed to the
22 λ_{max} at ~ 256 nm. Previous study¹⁰³ report the UV-vis spectra of Fe^{II} - tannic acid complexes at
23 acidic pH absorbing closer to 260 nm, while Fe^{II} -cationic complexes in aprotic solutions exhibit a
24 unique and narrow λ_{max} at 262 nm.¹⁰⁴ The photochemical mechanism of the Fe^{III} -citrate system
25 (scheme I) explains the evolution of the $MAC(\lambda)_{bulk}$ spectra observed in our experiment.
26 Specifically, the initial photolysis of Fe^{III} -citrate ($R \rightarrow I$ reactions) proceeds through rapid ligand to
27 metal charge transfer (LMCT) excitation,¹⁰⁵ reducing Fe^{3+} to Fe^{2+} and dissociating and oxidizing
28 the citrate-radical pair.³¹ Reduced Fe^{2+} products exist as intermediate species; they are oxidized
29 back to Fe^{3+} ($I \rightarrow P$ reactions) at the longer photolysis times in the presence of ROS species and
30 dissolved oxygen. The formal kinetics and modeled curves describing relative fractions of R , I ,
31 and P components in the photoreacting system shown in Figure 1c indicate a net apparent effect
32 of reactions similar to R1-9 (Scheme 1). To validate our assumption that I products are indeed
33 associated with Fe^{II} intermediates, we measured dissolved $[Fe^{2+}]$ concentrations at selected
34 irradiation times. The Fe^{2+} concentration is low in the unreacted sample (3.8 μM), which is close
35 to the limit of detection (~ 2.3 μM). As the photolysis progresses to 5 min, the averaged
36 concentration of dissolved Fe^{2+} increases to 55.3 μM , then gradually decreases to 25-12 μM at 20-
37 40 min and to 7-3 μM at 80-120 min, respectively. Figure 1c shows that overall concentrations of
38 Fe^{2+} ions in the solutions (brown triangles) agree well with the modeled time-resolved profile of
39 the intermediate products I (brown dashed lines). The processes influencing $[Fe^{2+}]$ production are
40
41
42
43
44
45
46
47
48
49
50
51
52
53
54
55
56
57
58
59
60

1
2
3 related to (1) dissociation of citrate ligand from Fe^{III} center and reduction following LMCT as
4 previously mentioned.^{31,105} (2) The reactions and rate of reactions of available ROS (i.e. H₂O₂, O₂,
5 and HO₂) in the solution with dissolved Fe²⁺ and (3) speciation of Fe(II) in the aqueous solution at
6 the higher pH (~6.5 - 6.7) ranges where peroxides react with photoreduced Fe²⁺ and re-oxidize
7 back to Fe³⁺, significantly faster than at the lower pH conditions in separate studies.^{43,62,106}
8
9

10
11 The apparent quantum yield, Φ of the generalized photochemical decomposition of R (Fe^{III}-citrate
12 reactant) was calculated based on the observed number of reacted Fe^{III}-citrate molecules divided
13 by the number of photons to which the experimental solutions were exposed. The latter was
14 calculated based on the photon flux measured in the actinometry experiments (Appendix B in SI
15 file). The calculated apparent Φ is ~ 0.02, which is only ~10% of the intrinsic Φ values reported
16 in the range of ~ 0.16 – 0.30 for Fe^{III}-carboxylates.^{25,61} Lower values of the apparent Φ are a
17 combined result of additional absorbance and scattering by other components in the reaction
18 mixture, which evolve over the reaction time. Therefore, apparent first-order reaction rates of $j_1=$
19 0.12 min⁻¹ and $j_2=$ 0.05 min⁻¹ obtained from the formal kinetic modeling need to be considered as
20 specific to our experimental conditions. Details of the kinetic model are described in Appendix E
21 of the SI file. For the extrapolations of kinetic data to experiments external to our study, the
22 apparent rates and the apparent Φ need to be considered together, scalable to the relevant Φ values
23 determined in the corresponding experiments.
24
25
26
27
28
29
30
31
32
33
34

35
36 **Molecular Characterization of the Irradiated Samples.** Figure 2a illustrates HPLC-PDA
37 experimental results showing separated components of Fe^{III}-citrate solutions irradiated for 0, 5, 40,
38 80, and 120 min. For our analysis, the major separated absorbing components eluted between 0 –
39 3 min RT unretained period and 3 – 12 min RT for weakly to strongly retained species. Therefore,
40 we discuss those identified within these two LC ranges. The individual features are labeled
41 accordingly in each of the respective panels as reactants (R_i), intermediates (I_i), and products (P_i),
42 with their respective coloring schemes from Figure 1c describing the $R \rightarrow I \rightarrow P$ progression. In
43 total, 31 individual HPLC-PDA features (~ 95% of all features) are detected and identified in 5
44 irradiated samples based on the correlative assessment of HPLC-PDA and HPLC-ESI(-)/HRMS
45 records. Table 1 includes a list of separated features and proposed structures commonly grouped
46 with R_x , I_y , and P_z components, whereas the full list of separated features with corresponding
47 retention times, UV-vis spectra, and HRMS information are reported in Table S1 of the SI file.
48
49
50
51
52
53
54
55
56
57
58
59
60

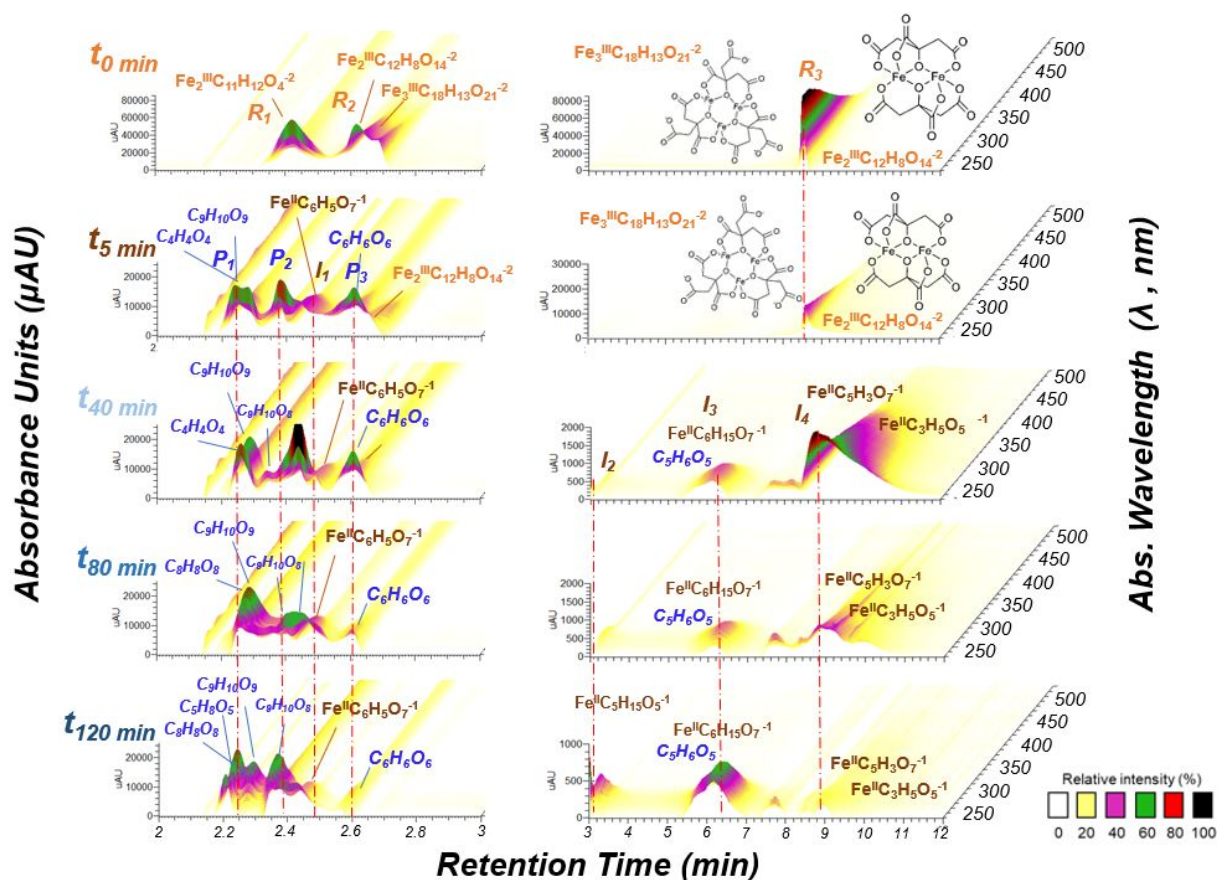
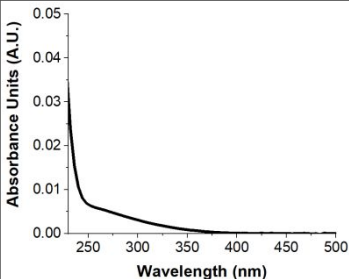
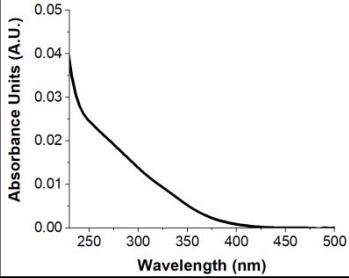
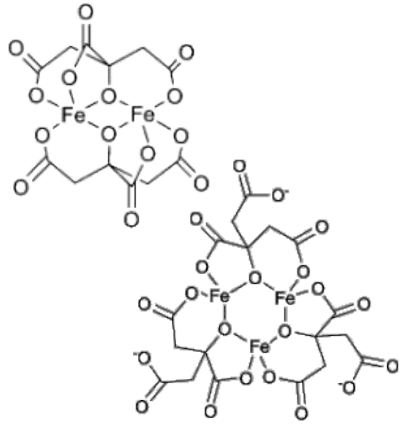
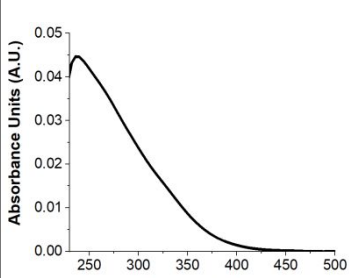


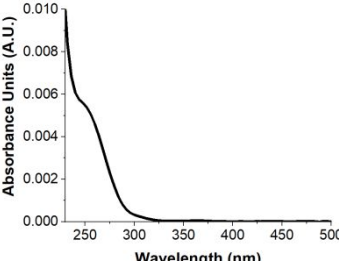
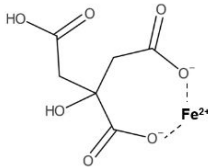
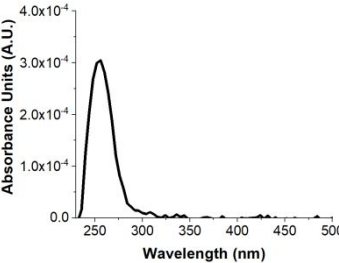
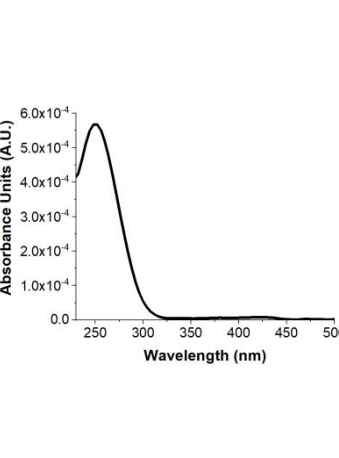
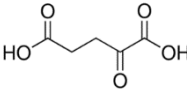
Figure 2. HPLC-PDA chromatograms of individually separated components formed in irradiated Fe^{III}-citrate solutions at 0, 5, 40, 80, and 120 min. The x-axis is retention time, y-axis is UV-vis absorbance and z axis is wavelength. Color indicates relative absorbance as depicted by the color map at the bottom. Assigned formulas corresponding to organic compounds (CHO-) recorded here as neutral molecules, whereas Fe-organic compounds denoted as corresponding ions.

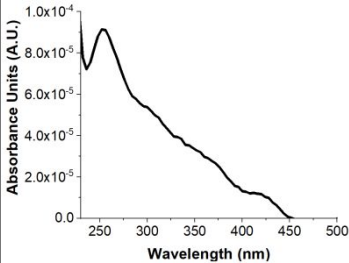
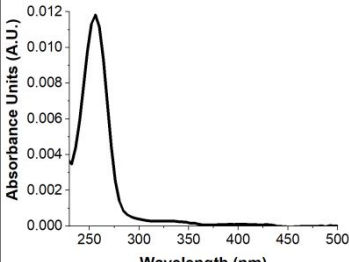
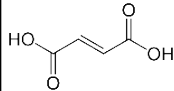
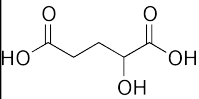
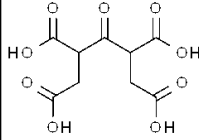
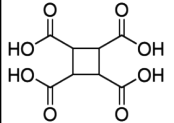
The molecular components of the unreacted solution show three HPLC-PDA features at 2.4, 2.7 and 8.7 min RT, marked as R_1 , R_2 and R_3 , respectively. Analysis of the corresponding HRMS datasets revealed deprotonated ions $[M-H]^-$ of $^{56}\text{Fe}_2^{\text{III}}\text{C}_{11}\text{H}_{12}\text{O}_4^{-2}$, $^{56}\text{Fe}_3^{\text{III}}\text{C}_{18}\text{H}_{13}\text{O}_{21}^{-2}$, $^{56}\text{Fe}_3^{\text{III}}\text{C}_{18}\text{H}_{15}\text{O}_{22}^{-2}$, and $^{56}\text{Fe}_3^{\text{III}}\text{C}_{12}\text{H}_{10}\text{O}_{14}^{-2}$ eluted at the corresponding time of R_2 and R_3 , which collectively represent the dinuclear dicitrate (Fe_2Cit_2), trinuclear tricitrate (Fe_3Cit_3 & $\text{Fe}_3\text{Cit}_3\text{O}$), and trinuclear dicitrate (Fe_3Cit_2) complexes, respectively.^{73,74,84} The R_1 feature corresponds to $[M-H]^-$ of $^{56}\text{Fe}_2^{\text{III}}\text{C}_{11}\text{H}_{12}\text{O}_4^{-2}$. Detection of this Fe-containing peak did not correspond to any of the Fe_xCit_y complexes observed here, nor in previous studies. It is assumed that this is likely a chemical impurity of the Fe^{III}-citrate chemical used in the study. Detection of their characteristic ^{54}Fe

1
2
3 isotopes in the integrated MS spectra explicitly confirmed molecular assignments of the Fe-
4 containing ions. Extracted ion chromatograms of the Fe^{III}-citrate complexes overlaid with the LC-
5 PDA chromatographic peaks are illustrated in Figure S4 of the SI file. Details of DI-ESI(-)/HRMS
6 and ESI-MS² characterization of all Fe-containing peaks in the unreacted sample are described in
7 Figures S5, S6 and Table S2 of the SI file. After 5 min of photolysis, all *R* features decrease
8 substantially, indicating their lower concentrations. We estimate the summed concentration of
9 Fe^{III}-citrate complexes (*R*₂ and *R*₃) from the HPLC-PDA measurement based on the literature
10 reported molar extinction coefficient at $\lambda = 365$ nm ($\epsilon = 900$ L mol⁻¹ cm⁻¹)¹⁰⁷ to be ~ 78.4 and 1.4
11 μ M for 0 and 5 min samples, respectively. Considering that this concentration of the Fe^{III}-citrate
12 complexes in the unreacted mixture is lower than concentration of the dissolved Fe^{III}-citrate salt
13 ($\sim 90\mu$ M), the remaining 11.6μ M likely corresponds to un-complexed/un-dissolved [Fe]³⁺,
14 [citrate]³⁻ ions, and surface-bound Fe^{III}-citrate complexes on the high surface area iron oxide (i.e.
15 FeOOH) colloids in the solution.¹⁰⁸ At the relevant Fe concentrations used in this study, formation
16 of insoluble iron oxide colloids precipitated in the aqueous solution at the higher pH setting
17 form.¹⁰⁹ For mechanistic interpretation of Fe(III)-citrate photochemical degradation discussed
18 here, special consideration of multi-phase photoreductive dissolution processes of colloidal
19 surface-bound Fe^{III}-citrate and other Fe-organic complexes in the aqueous solution should be
20 accounted for.^{108,110–112} The photodegradation of oxide bound Fe^{III}-citrate complexes lead to
21 dissolution of Fe^{III}-citrate, followed by Fe(III) reduction and immediate release of soluble Fe²⁺ and
22 citrate from colloid to the aqueous solution.¹⁰⁸ Overall, photodegradation of the soluble and surface
23 bound Fe^{III}-citrate complexes initiated through LMCT reactions³¹ R1-R4 (Scheme 1) is very fast,
24 resulting in rapid reduction of Fe^{III} to Fe^{II} over the first 5 min of photolysis. *R* components were
25 not detected in the samples collected at longer irradiation times.
26
27
28
29
30
31
32
33
34
35
36
37
38
39
40
41
42
43
44
45
46
47
48
49
50
51
52
53
54
55
56
57
58
59
60

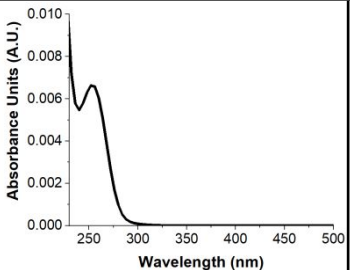
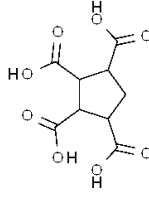
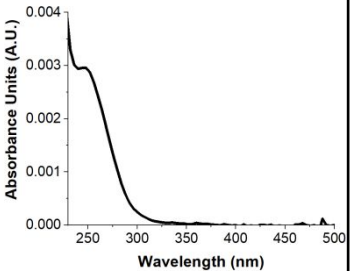
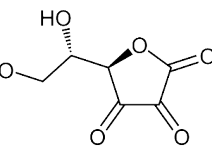
Table 1: Summary table of identified components in LC-PDA-HRMS datasets.

ID	RT (min)	UV-Vis Spectrum	Exp. m/z	Chemical Formula	Mass Error (ppm)	Proposed Structure & Description
			(-)ESI			
<i>Reactants (R_i)</i>						
<i>R₁</i>	2.3		159.972	$\text{Fe}_2^{\text{III}}\text{C}_{11}\text{H}_{12}\text{O}_4^{-2}$	1.875	
<i>R₂</i>	2.6		366.401 375.406 243.931 488.870 271.899	$\text{Fe}_3^{\text{III}}\text{C}_{18}\text{H}_{13}\text{O}_{21}^{-2}$ $\text{Fe}_3^{\text{III}}\text{C}_{18}\text{H}_{15}\text{O}_{22}^{-2}$ $\text{Fe}_2^{\text{III}}\text{C}_{12}\text{H}_8\text{O}_{14}^{-2}$ $\text{Fe}_2^{\text{III}}\text{C}_{12}\text{H}_9\text{O}_{14}^{-1}$ $\text{Fe}_3^{\text{III}}\text{C}_{12}\text{H}_{10}\text{O}_{14}^{-2}$	0.689 0.533 0.152 0.466 0.345	 <i>Iron(III)-citrate (Fe:Cit) complexes based on previous literature, Fe isotope distribution, and optical signals/UV-vis spectra.^{74,113}</i>
<i>R₃</i>	8.4		366.400 375.406 243.931 488.870 271.898	$\text{Fe}_3^{\text{III}}\text{C}_{18}\text{H}_{13}\text{O}_{21}^{-2}$ $\text{Fe}_3^{\text{III}}\text{C}_{18}\text{H}_{15}\text{O}_{22}^{-2}$ $\text{Fe}_2^{\text{III}}\text{C}_{12}\text{H}_8\text{O}_{14}^{-2}$ $\text{Fe}_2^{\text{III}}\text{C}_{12}\text{H}_9\text{O}_{14}^{-1}$ $\text{Fe}_3^{\text{III}}\text{C}_{12}\text{H}_{10}\text{O}_{14}^{-2}$	0.307 0.134 0.152 0.998 1.530	
<i>Intermediates (I_i)</i>						

I_1	2.4		244.939	$\text{Fe}^{\text{II}}\text{C}_6\text{H}_5\text{O}_7^{-1}$	1.48	 <p><i>Iron(II)Citrate based on spectral database match and isotope distribution.¹¹⁴</i></p>
I_2	3.1		211.028	$\text{Fe}^{\text{II}}\text{C}_5\text{H}_{15}\text{O}_5^{-1}$	3.2	
			197.012	$\text{Fe}^{\text{II}}\text{C}_4\text{H}_{13}\text{O}_5^{-1}$	3.2	
I_3	6.2		255.018	$\text{Fe}^{\text{II}}\text{C}_6\text{H}_{15}\text{O}_7^{-1}$	2.01	
			211.028	$\text{Fe}^{\text{II}}\text{C}_5\text{H}_{15}\text{O}_5^{-1}$	3.2	
			145.014	$\text{C}_5\text{H}_6\text{O}_5$	0.37	 <p><i>Alpha-ketoglutaric acid</i></p>
I_4	8.8		230.923	$\text{Fe}^{\text{II}}\text{C}_5\text{H}_3\text{O}_7^{-1}$	0.23	
			190.965	$\text{Fe}^{\text{II}}\text{C}_4\text{H}_7\text{O}_5^{-1}$	0.58	

			176.949	$\text{Fe}^{\text{II}}\text{C}_3\text{H}_5\text{O}_5^{-1}$	0.79	
<i>Products (P_i)</i>						
<i>P₁</i>	2.2		115.004	$\text{C}_4\text{H}_4\text{O}_4$	0.853	 <i>Fumaric acid</i>
			147.029	$\text{C}_5\text{H}_8\text{O}_5$	0.200	 <i>2-hydroxyglutaric acid</i>
			261.025	$\text{C}_9\text{H}_{10}\text{O}_9$	0.594	 <i>3-oxo-1,2,4,5-pentanetetracarboxylic acid</i>
<i>P₂</i>	2.3		231.015	$\text{C}_8\text{H}_8\text{O}_8$	0.431	 <i>cyclobutanetetracarboxylic acid</i>

1
2
3
4
5
6
7
8
9
10
11
12
13
14
15
16
17
18
19
20
21
22
23
24
25
26
27
28
29
30
31
32
33
34
35
36
37
38
39
40
41
42
43
44
45
46
47

		 <p>Absorbance Units (A.U.)</p> <p>Wavelength (nm)</p>	245.030	$C_9H_{10}O_8$	0.451	 <p><i>cyclopentanecarboxylic acid</i></p>
P_3	2.6	 <p>Absorbance Units (A.U.)</p> <p>Wavelength (nm)</p>	173.009	$C_6H_6O_6$	0.122	 <p><i>Dehydroascorbic acid</i></p>

The identified HPLC-PDA features eluting at RTs of 2.4, 3.1, 6.2, and 8.8 min in the samples from 5 and 40 min irradiation times correspond to Fe^{II}-organic intermediates I_1 , I_2 , I_3 , and I_4 , respectively. I_1 is plausibly identified as the reduced mono-charged Fe^{II}-citrate complex, corresponding to $^{56}\text{Fe}^{\text{II}}\text{C}_6\text{H}_5\text{O}_7^{1-}$, which is chemically different than the Fe^{III}-citrate complex(es) observed as R species. Fe^{II}-citrate was detected in all of the photoreacted samples. Extracted ion chromatograms for both $^{56}\text{Fe}^{\text{II}}\text{Cit}$ and $^{56}\text{Fe}_2^{\text{III}}\text{Cit}_2$ complexes eluting at different retention times along with corresponding UV-visible spectra recorded by PDA detector are described in Figure S7 of the SI file. The complexation of Fe²⁺ to citric acid occurs at neutral and alkaline pH conditions (within LC buffer ranges), as the hydroxyl groups in citrate molecule become ionized in solution forming the monomeric Fe^{II}-citrate complex.¹¹⁵ Our results show that Fe^{II}-citrate and Fe^{III}-citrate are uniquely identifiable and distinguishable in these LC experiments. However, those species are considered unstable and relatively weak complexes in the aqueous solution¹¹⁶; therefore it is difficult to quantify Fe^{II}-citrate (aq) in these experiments. Nevertheless, to the best of our knowledge, separated and distinguished Fe^{III}- and Fe^{II}-citrate complexes are shown here for the first time. Detection of these Fe^{II}-citrate intermediates implies that a fraction of these species did not degrade immediately following LMCT conversion of both soluble and oxide bound¹⁰⁸ Fe^{III}-citrate complexes to Fe²⁺ and citrate ions. I_2 corresponds to two coeluting monocharged Fe-organic complexes of $^{56}\text{Fe}^{\text{II}}\text{C}_5\text{H}_{15}\text{O}_5^{1-}$ and $^{56}\text{Fe}^{\text{II}}\text{C}_4\text{H}_{15}\text{O}_5^{1-}$ while I_3 corresponds to a mixture of two ions: $^{56}\text{Fe}^{\text{II}}\text{C}_6\text{H}_{15}\text{O}_7^{1-}$ monocharged complex and α -ketoglutaric di-carboxylic acid ($\text{C}_5\text{H}_6\text{O}_5$), which was reported in a previous study²⁵ as an abundant organic intermediate in the photodecomposition of Fe^{III}-citrate. Finally, strongly absorbing I_4 feature corresponds to several co-eluting mono-charged ions: $^{56}\text{Fe}^{\text{II}}\text{C}_3\text{H}_5\text{O}_5^{1-}$, $^{56}\text{Fe}^{\text{II}}\text{C}_4\text{H}_7\text{O}_5^{1-}$, and $^{56}\text{Fe}^{\text{II}}\text{C}_5\text{H}_3\text{O}_7^{1-}$, which exhibit maximum absorbance at $\sim 250 - 256$ nm and tailing in the 350 – 400 nm ranges (see Table 1 and Table S1 of SI file). Consistently with the observed $R \rightarrow I \rightarrow P$ formal kinetics, all I features identified here degrade substantially at longer irradiation times and are therefore poorly seen in the 80 and 120 min samples. The degradation of Fe(II) intermediate species here is likely due to the oxidation of Fe²⁺ back to Fe³⁺ in the presence of citrate and available oxygen at the relevant pH conditions similar to previous work.¹¹⁷ The rate of Fe(II)-citrate oxidation is enhanced in the presence of high concentrations of citrate in the solution,¹¹⁸ therefore we should expect the rate of Fe(II) oxidation to be proportional to the concentration of citrate ions in the solution.

1
2
3 Features P_1 , P_2 , and P_3 , eluting at 2.2, 2.3, and 2.6 min RT were detected in each of the irradiated
4 mixtures. However, they become most abundant in the 80 and 120 min samples. The plausible
5 identification of P_1 is a mixture of co-eluting organic compounds such as fumaric acid ($C_4H_4O_4$),
6 2-hydroxyglutaric acid ($C_5H_8O_5$), and 3-oxo-1,2,4,5-pentanetetracarboxylic acid ($C_9H_{10}O_9$), while
7 P_2 feature is associated with cyclobutanetetracarboxylic ($C_8H_8O_8$) and cyclopentane carboxylic
8 ($C_9H_{10}O_8$) acids. Detection of small organic acid byproducts such as fumaric (C_4) and hydroxy
9 glutaric acid (C_5) in the irradiated mixtures results from decarboxylation of citrate radical in the
10 presence of oxygen (R4 in Scheme 1). In addition, plausible Norrish I and II photodegradation
11 pathways (R10-11 in Scheme 1) are the source of small organic acids with C=C double bonds and
12 other radical recombinant species (R-R). Photolysis of citric acid by OH^\bullet mediated heterogenous
13 oxidation in a separate study¹¹⁹ results in extensive fragmentation of C-C bonds through acid-base,
14 free-radical chemical reactions, as well as decarboxylation and formation of carboxyl and
15 carbonyl-groups. Therefore, fumaric acid, 2-hydroxy glutaric acid and other small molecules are
16 expected byproducts of the decarboxylation and they are also common enzymatic metabolites in
17 the citric acid ‘Krebs’ cycle.¹²⁰ Alternatively, detection of highly oxygenated multi-carboxylic
18 acid and hydroxy dimers in this photolyzed system, such as $C_7H_8O_8$, $C_8H_{10}O_9$, and $C_{10}H_{12}O_{10}$, are
19 consistent with a previous study investigating the heterogenous photooxidation of dicarboxylic
20 acids catalyzed on the surface of TiO_2/Fe_2O_3 dust particles.¹²¹ Carboxylic dimer products can arise
21 from radical-radical recombination reactions (R9-10 in Scheme 1) of two carboxylic monomer
22 radicals in the irradiated solution. Lastly, HPLC feature P_3 eluting at 2.6 min RT corresponds
23 plausibly to dehydroascorbic acid ($C_6H_6O_6$), a cyclic molecule with multiple carbonyl (C=O)
24 groups and two hydroxyl groups. The characteristic absorption profile of this molecule is similar
25 to that reported in previous study¹²² investigating similar species and ascorbic acid via HPLC-
26 PDA. However, this molecule may also undergo consequent Norrish photochemistry or
27 reactions¹²³ with H_2O_2 to yield other oxidized, ring-opening products such as $C_6H_8O_8$ detected in
28 the irradiated samples. Full list of identified CHO-containing species is included in Table S3 of
29 the SI file. Overall, cyclic Fe redox reactions in the solution catalyzes the oxidation of citrate to
30 several of the intermediate and product species representing structurally similar species.
31
32
33
34
35
36
37
38
39
40
41
42
43
44
45
46
47
48
49
50
51
52
53
54
55
56
57
58
59
60

1
2
3 **Optical Properties of the Irradiated Samples** Figure 3 illustrates contributions of individual *R*,
4 *I* and *P* components to $MAC(\lambda)_{\Sigma}^{PDA}$ spectra recorded by HPLC-PDA for each of the five analyzed
5 samples. Overall, the systematic and quantitative changes in the absolute values of $MAC(\lambda)_{\Sigma}^{PDA}$
6 and the relative fractions of *R*, *I* and *P* contributions can be observed as the photolysis reactions
7 progress. Components *R* dominate absorbance in the unreacted sample. Their contribution is
8 halved in the sample irradiated for 5 min, where contributions by the *R* and *I* components become
9 nearly equal, and influence of the *P* components also becomes detectable. At the later irradiation
10 times (40 – 120 min), contributions from *P* continue to grow, while contributions from *I* decline
11 and contributions from *R* are undetectable. Notably, absolute values of $MAC(\lambda)_{\Sigma}^{PDA}$ decline
12 steadily as the photolysis reactions proceed and the spectral shape changes from featureless to
13 more defined with a well-distinguished peak at 256 nm. At 80 – 120 min irradiation time, the
14 $MAC(\lambda)_{\Sigma}^{PDA}$ values decrease by a factor of ~ 5 compared to those measured for the unreacted
15 sample. These observations are in striking contrast to the $MAC(\lambda)_{bulk}$ measurements using a UV-
16 vis spectrophotometer shown in Figures 1a and 1b. While both measurements show the same trend
17 of the *MAC* declining during the photolysis, absorption detected by the UV-vis spectroscopy of
18 bulk samples is much higher than that inferred from the HPLC-PDA measurements of the same
19 samples. The plausible reason for this discrepancy is a difference in the analyte material probed in
20 two measurements. Specifically, the $MAC(\lambda)_{bulk}$ spectra reflect absorption by total organic carbon
21 (TOC) which includes dissolved water-soluble organic carbon (WSOC) and colloids, while the
22 $MAC(\lambda)_{\Sigma}^{PDA}$ spectra correspond to the light absorption by WSOC only. Therefore $MAC(\lambda)_{\Sigma}^{PDA} \stackrel{def}{=} MAC(\lambda)_{\Sigma}^{WSOC}$.

23
24
25
26
27
28
29
30
31
32
33
34
35
36
37
38
39
40
41
42
43
44
45
46
47
48
49
50
51
52
53
54
55
56
57
58
59
60

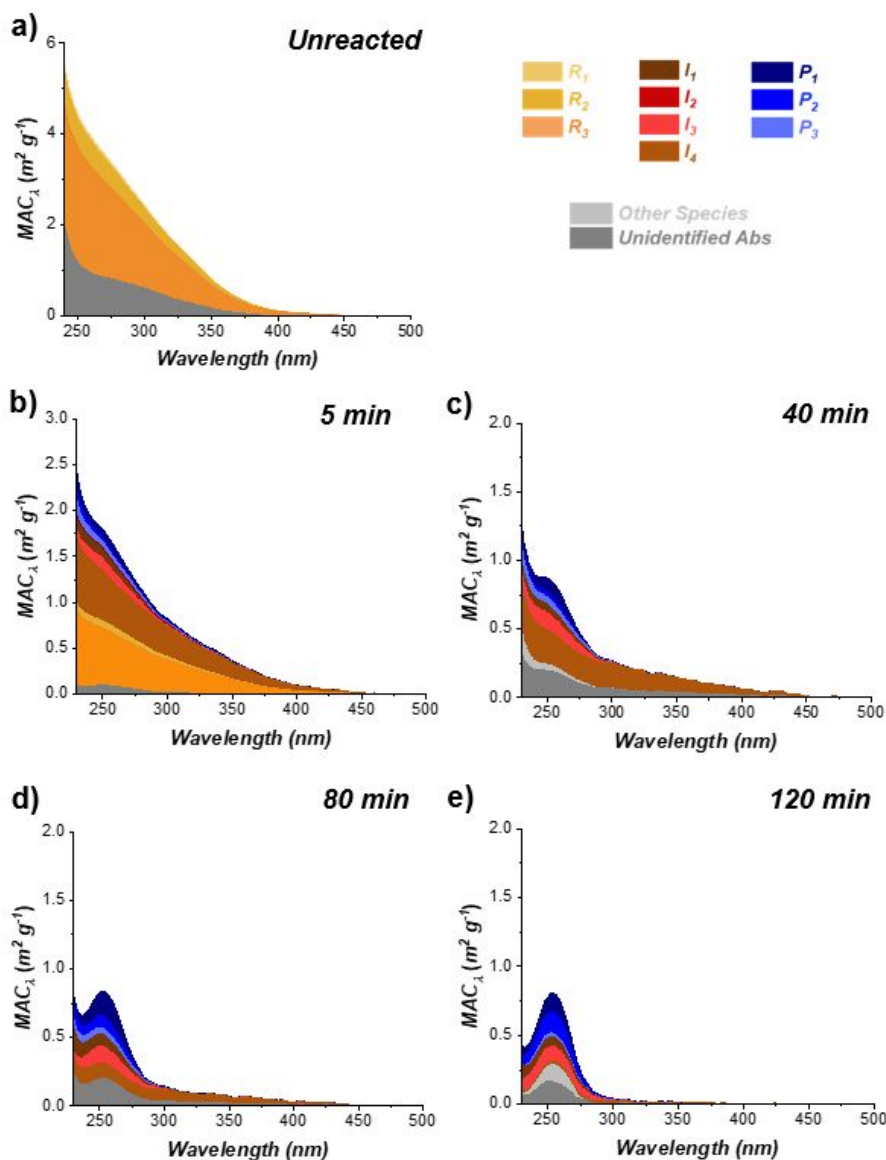
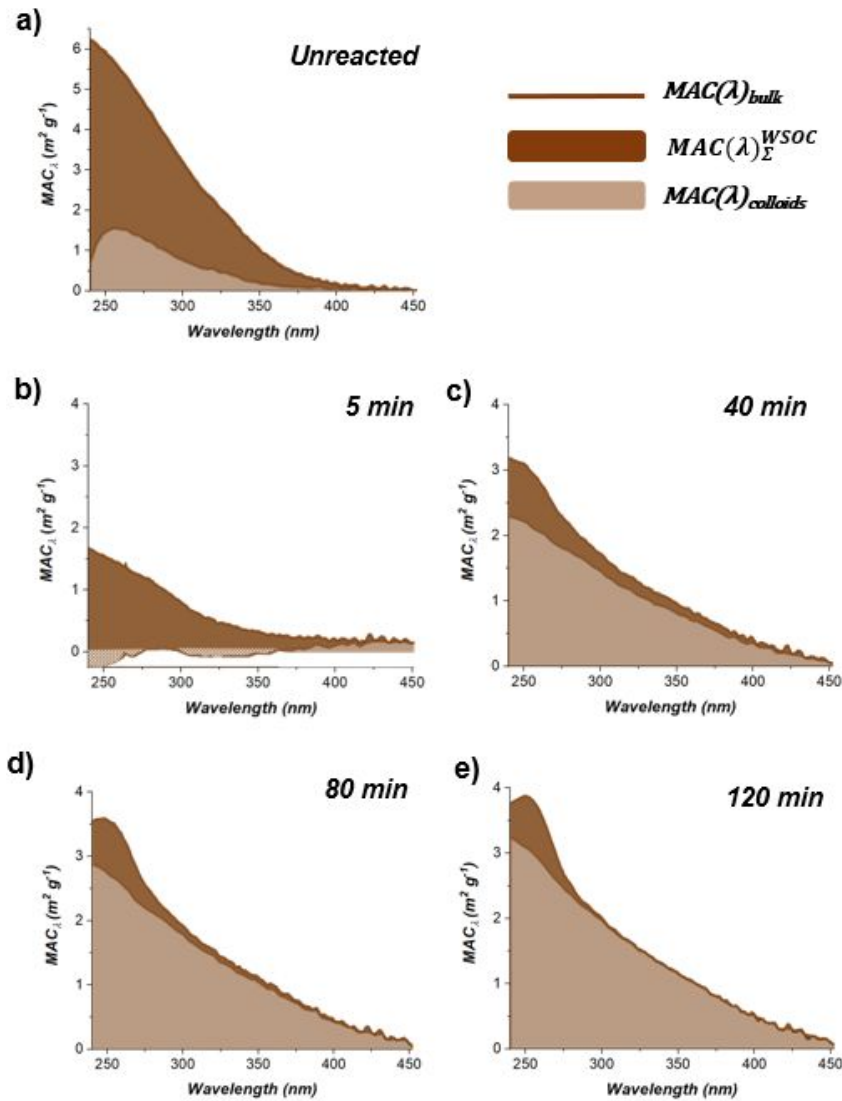


Figure 3: Fractions of $MAC(\lambda)_{\Sigma}^{PDA}$ attributed to water-soluble individual components of the Fe^{III} -citrate irradiated mixtures. Orange, brown, and blue colors indicate contributions from reactants (R), intermediates (I), and products (P) defined in Figure 2.

Figure 4 further illustrates the relationship between $MAC(\lambda)_{bulk}$ and $MAC(\lambda)_{\Sigma}^{WSOC}$ values determined for all 5 samples studied here. Individual panels illustrate relative fractions of $MAC(\lambda)_{\Sigma}^{WSOC}$ and $MAC(\lambda)_{colloids}$ out of $MAC(\lambda)_{bulk}$ spectra measured for the unreacted and irradiated samples. The $MAC(\lambda)_{\Sigma}^{WSOC}$ is the major fraction of $MAC(\lambda)_{bulk}$ for the unreacted and 5 min irradiated mixtures, suggesting only minor effects of colloids (likely $Fe(OH)_3$) at the beginning of reaction. At later irradiation times (40-120 min), the buildup of colloidal products is

1
 2
 3 evident from increased values of $MAC(\lambda)_{colloids} = MAC(\lambda)_{bulk} - MAC(\lambda)_{\Sigma}^{WSOC}$ illustrated in the
 4 plots. The $MAC(\lambda)_{colloids}$ absorbing fraction in these mixtures is presumably related to formation of
 5 insoluble $Fe(OH)_3$ and poorly soluble reduced carbon products of reactions R12 (Scheme 1) that
 6 contribute to formation and growth of colloids. To test this assumption, we conducted a focused
 7 study to provide insights on the sizes, concentration, and chemical composition of these colloidal
 8 products.
 9
 10
 11
 12
 13
 14
 15
 16
 17
 18
 19
 20
 21
 22
 23
 24
 25



50 **Figure 4.** The relative fractions of $MAC(\lambda)_{\Sigma}^{WSOC}$ and $MAC(\lambda)_{colloids}$ out of $MAC(\lambda)_{bulk}$ spectra measured
 51 for the samples analyzed in this study.
 52
 53
 54
 55
 56
 57
 58
 59
 60

1
2
3 ***In Situ* Flow Microscopy Detection of Colloids** Colloidal components of the unreacted and
4 irradiated samples at 5, 40, 80, and 120 min were measured using the FlowCam® Nano oil
5 immersion flow microscope that is capable to image and count individual colloidal particles larger
6 than 0.3 μm . Figures 5a-5e shows the 8-bin per decade number size distributions ($\Delta N/\Delta \log D_p$;
7 particles cm^{-3}) for the unreacted, 5 min, 40, 80 min, and 120 min photoreacted samples. In the
8 unreacted sample, the particle number concentration is low. The representative particle images
9 (included in Figure S8 of the SI file) reveal relatively smaller and round colloidal particles in the
10 unreacted system, which are likely commonly occurring $\text{Fe}(\text{OH})_3$ colloids and the presumed oxide
11 bound Fe^{III} -citrate particles. As the photolysis progresses from 5 – 120 min, the number
12 concentrations and size distributions of the particles detected grow in the reacted solutions, which
13 reveal significantly larger and more fractional colloids, as shown in Figure S8 of the SI file. The
14 estimated mass loadings shown in Figure 5f indicate progressive increase from $<50 \mu\text{g/L}$ in the
15 unreacted sample to $>1000 \mu\text{g/L}$ in the irradiated samples. Ranges of lower and upper mass limits
16 are shown to reduce bias of larger particles ($> 3 \mu\text{m}$) that are sparsely present. Details of the data
17 analysis are described in Appendix F of the SI file. With respect to the unreacted sample, the mass-
18 size distributions are shifted to larger particle sizes, suggesting that reduced carbon components
19 formed after prolonged photolysis contribute to the buildup of colloids in the irradiated samples
20 (see Figure S9 of the SI file). The mass loading of colloids in the 80 and 120 min irradiated sample
21 corresponds to $\sim 8\%$ and 5% of the original $\text{Fe}(\text{III})$ -Cit reactant mass. However, particles within
22 the $0.3 - 0.5 \mu\text{m}$ size ranges contribute most to the observed scattering of UV-visible light in the
23 near visible regions of the absorption spectrum shown in Figure 1a. Nevertheless, these results
24 show the formation of new colloids that effectively increase in concentration under prolonged
25 irradiation to UV-Vis light, representing an important pathway to nanoparticle products formation
26 in photochemical Fe^{III} -carboxylate systems.
27
28
29
30
31
32
33
34
35
36
37
38
39
40
41
42
43
44
45
46
47
48
49
50
51
52
53
54
55
56
57
58
59
60

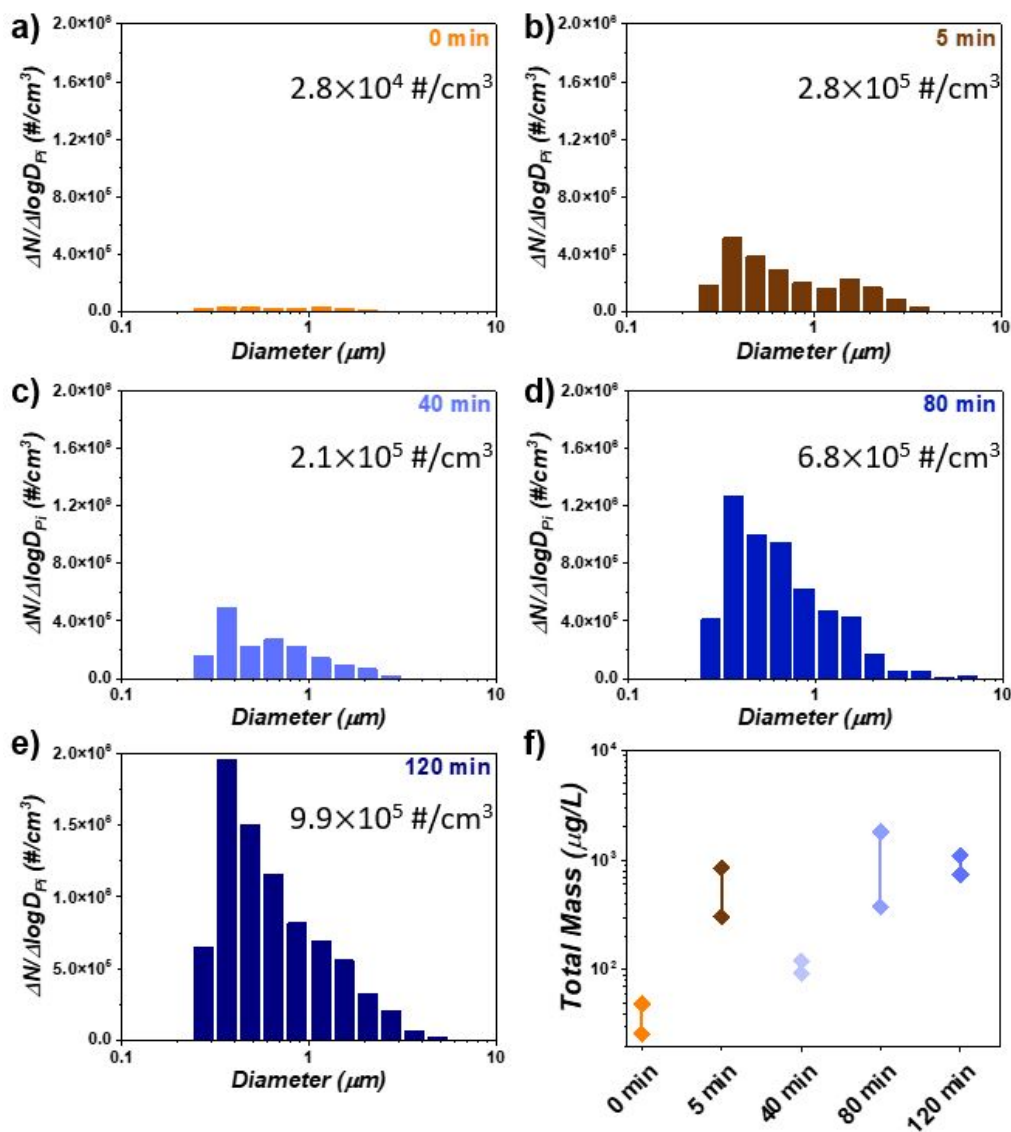


Figure 5. Particle number size distribution of colloids detected in the unreacted (orange) and photoreacted samples at 5 (brown), 40, 80, and 120 min (light blue - dark blue). Diameter reported by the flow microscope is the equivalent size diameter (ESD) in μm . Calculated mass loadings for each of the cases are reported as upper and lower limit values in panel f (see Fig S9 for additional details).

Chemical Characterization of Colloidal Material Colloidal material found in the 120 min irradiated sample was used for chemical characterization. Extracted colloidal material was dissolved in the ‘org-mix’ solvent and the obtained solutions were analyzed in DI-ESI(+)-HRMS

1
2
3 experiments for detection of high molecular weight components formed from radical
4 recombination (R12 of Scheme 1). Figure 6a illustrates results of the ESI(+)-HRMS analysis,
5 indicating MS features identified and assigned in the 500-1100 Da mass range. The representative
6 inset plot in Figure 6a illustrates selected CHO peaks and their formula assignments in the 650-
7 730 m/z range. Figure 6b and 6c show the hydrogen-to-carbon (H/C) elemental ratios and DBE of
8 species found in colloidal components, plotted as a function of number of carbon atoms (C) and
9 color-coded by their oxygen-to-carbon (O/C) ratio (Figure 6b). Reference lines in Figure 6c
10 correspond to cata-PAH's ($DBE = 0.75 \times C - 0.5$)¹²⁴ and linear conjugated polyenes C_xH_x+2 (DBE
11 $= 0.5 \times C$).¹²⁵ The molecular species representative of dissolved colloids in this HRMS dataset
12 span 30 – 60 carbon atoms with varying degree of oxygenation and unsaturation due to double
13 bonds in the organic structures. The adsorbed components of the colloidal material is composed
14 of moderately saturated aliphatic and unsaturated hydrocarbon species with variable DBE and low
15 oxygen content. Majority of the assigned features with higher HRMS signal intensity fall below
16 the linear conjugated polyene boundary line, while some of the lower intensity features fall closer
17 to the condensed aromatic reference line. Few selected species such as: $C_{34}H_{64}O_{11}$ ($DBE = 3$; O/C
18 $= 0.32$), $C_{37}H_{56}O_{12}$ ($DBE = 10$; $O/C = 0.32$), $C_{40}H_{62}O_8$ ($DBE = 10$; $O/C = 0.2$), $C_{47}H_{58}O_5$ ($DBE =$
19 19 ; $O/C = 0.11$), and $C_{49}H_{54}O_5$ ($DBE = 23$; $O/C = 0.1$) represent less oxygenated/ more reduced
20 carbon fragments that were adsorbed on colloid surfaces.
21
22
23
24
25
26
27
28
29
30
31
32
33
34
35
36
37
38
39
40
41
42
43
44
45
46
47
48
49
50
51
52
53
54
55
56
57
58
59
60

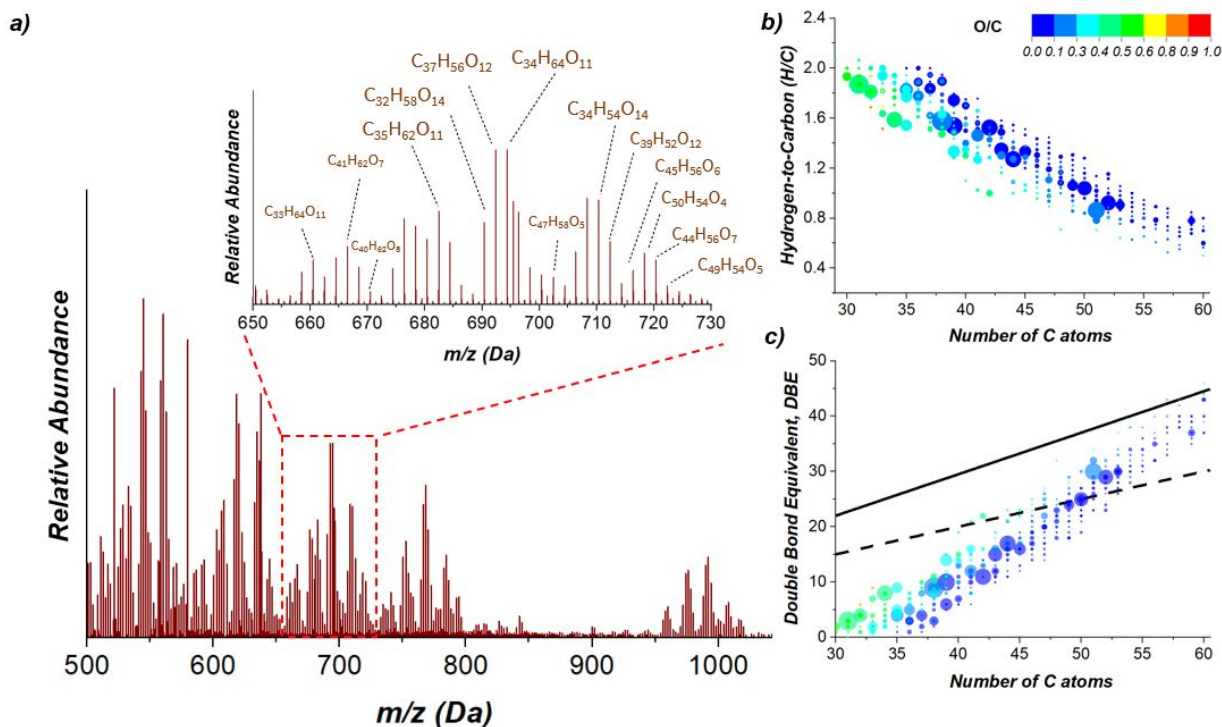


Figure 6. a) (+)ESI-HRMS spectrum representative of the ‘*org-mix*’ digested colloidal components identified in the Fe^{III}-citrate mixture irradiated for 120 min. Inset plot shows zoomed in HRMS spectrum in the range 650-730 Da, b) H/C ratio vs number of carbon atoms (C) plot and c) DBE vs C plot scaled to O/C ratio. Reference lines represent DBE values of linear polyenes (dotted line; $0.5 \times C$)¹²⁵ and condensed aromatics (dashed line; $0.75 \times C - 0.5$).¹²⁴ The size of all individual symbols is scaled to the square root of the MS peak intensity.

Overall, we observe unique low and high molecular weight features in the mixture comprising dissolved colloid fragments composed of C, H and O immediately following dissolution in ‘*org-mix*’ followed by ultrasonication. Of note, those features were only observed in the HRMS spectra of sonicated samples, confirming their apportionment to the degraded colloids (see Figure S9 of SI file for more details). Furthermore, those features were also absent in MS spectra acquired from the unreacted sample prepared following the same dissolution procedures (see Figure S10 of the SI file). Therefore, adsorbed colloidal analytes probed at the longer photolysis time are composed of less oxygenated (more reduced) carbon material, resulting from the radical recombination reactions in R12 of Scheme 1.

CONCLUSIONS

This study investigated multi-phase photochemistry of Fe-citrate and reported on the formation of unexplored colloidal products under prolonged light exposure. Apparent reaction rates of the $R \xrightarrow{j_1} I \xrightarrow{j_2} P$ formal kinetics derived from our experiments are $j_1 \sim 0.12 \text{ min}^{-1}$ and $j_2 \sim 0.05 \text{ min}^{-1}$, which correspond to the laboratory half-lifetimes of $\tau_{lab} \sim 8.3$ and 20 min, respectively (Appendix D). Scaling these half-lifetimes with respect to intensity of the solar radiation at summer solstice in Southern California and Mediterranean region suggests environmental half-lifetimes of ~ 32 min and ~ 1.3 hr, respectively. (Appendixes G and H). Therefore, we conclude that photochemical formation of colloidal products with carbon in a relatively reduced oxidation state may take place at the time scale relevant to the real-world environment of the Fe-carboxylate systems.

The light-absorbing properties of the photochemically reacting Fe-citrate mixtures are very much dynamic and overall comparable to those reported for atmospheric brown carbon (BrC). Figure 7 illustrates the $MAC(\lambda)_{bulk}$ values for the Fe-citrate samples of our study shown with respect to the optical-based AAE versus MAC_{405nm} classification framework.^{70,95,126,127} The light-absorbing properties of the unreacted and photoreacted Fe-citrate mixtures are skewed between weak (W) and moderate (M) light-absorbing classes, and they are less-absorbing than BrC from biomass burning.^{93,128} Over the course photochemical aging, BrC characteristics of the Fe-citrate mixture follows the $W \rightarrow M$ transition, resulting in stronger absorption by the photoreacted mixtures. This darkening is largely attributed to the carbonaceous colloidal material formed after prolonged photolysis under oxygen-deprived conditions. To date, no study has observed these systematic changes of Fe^{III}-carboxylates leading to production of insoluble carbonaceous colloids in aqueous photochemical reactions. To that extent, we therefore presume that formation of condensed reduced carbon species in this system is most likely similar to other extensively photolyzed brown carbon proxies,¹²⁹ and other Fe^{III}-carboxylate systems.^{20,24,34}

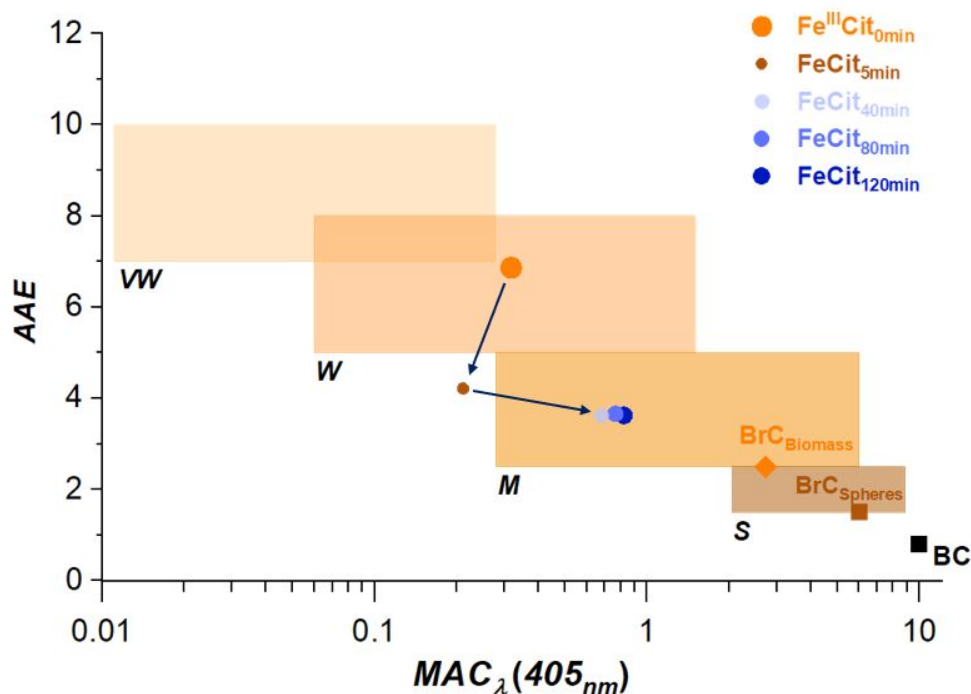


Figure 7. Optical properties of Fe-citrate photolysis samples mapped in the $AAE-MAC_{405\text{ nm}}$ space introduced by Saleh.¹²⁶ The shaded regions represent “optical bins” for “very weak (VW)”, “weak (W)”, “moderate (M)”, and “strong (S)” absorbing BrC classes. Literature-reported MAC values at 405 nm for BrC related to biomass burning,⁹³ spherical tar-balls,¹²⁸ and black carbon (BC)¹³⁰ are shown.

Overall, the results of this work demonstrate a multi-phase mechanism of the Fe^{III} -citrate photochemistry in aquatic systems of environmental relevance. The photochemical products identified in this representative Fe^{III} -carboxylate system are water-soluble components (R , I , and P components) and carbonaceous colloids formed under oxygen-deprived conditions in the extensively photolyzed mixtures. The detection of colloidal products in this system may contribute to yet unrecognized atmospheric and terrestrial light-absorbing material in aquatic environments with direct effects on the radiative forcing of climate. Further investigation of additional photoreactive Fe^{III} -carboxylate systems need to consider and account for formation of colloidal products that remain poorly characterized, overlooked in previous studies, and received little attention in the literature.^{62,131} In particular, ferric oxalate in natural aquatic environments may also behave similarly in the context of our work. Aqueous photolysis of ferric oxalate complex as shown in Figure S11 of the SI file follows similar trend, where degradation of $Fe(III)$ -oxalate complex occurs, followed by formation of short-lived $Fe(II)$ -intermediate species, and build-up of

1
2
3 water-soluble and insoluble colloidal reaction products where the light extinction extends beyond
4 500nm. Additionally, the aqueous photolysis of Fe-carboxylate complexes in natural waters are
5 important for Fe^{III/II} catalytic cycling, controlling the bioavailability of Fe(II) to microorganisms,¹³²
6 photo-mineralization of DOM, and oxidation of organic carbon in irradiated environmental waters
7 and in atmospheric aerosol particles.^{62,133–135}
8
9

10
11
12 Photoreactive Fe-carboxylates may also play an important role in initiating photocatalytic
13 reactions in snowpack. In particular, snow covered areas of inland central Asia^{127,136–138} located
14 near Fe^{III} dust sources may serve as an important medium for photocatalytic cycling of Fe^{III}-
15 carboxylates and the subsequent photooxidation of other water-soluble species (i.e. brown carbon,
16 carboxylic acids, ketones), halogenated species, and other inorganics in the snowpack. The
17 interactions of externally mixed Fe-mineral dust¹³⁷ and subsequent photochemical transformations
18 due to Fe^{III}-carboxylates can significantly enhance light absorption and modify the resulting snow
19 and surface albedo, with implications to indirect radiative forcing changes on the snow/surface
20 energy budgets. Specifically, carbonaceous colloid products resulted from Fe-carboxylate
21 photochemistry may accelerate melting of the snowpack, similar to BC and BrC deposits,¹³⁶
22 leading to reduction of the snow albedo.
23
24
25
26
27
28
29
30
31
32
33

34 SUPPORTING INFORMATION

35
36
37 Appendix A and Figure S1 describe transient optical and photochemical experimental setup of this
38 study; Appendix B and Figure S2 describes chemical actinometry experiments and relevant
39 calculations; Appendix C describes detailed direct infusion-HRMS parameters; Appendix D, E, F,
40 G, and H describes the formal kinetic modelling, quantum yields, particle size distributions,
41 atmospheric scaling, and TUV model calculations and selected parameters, respectively. Figure
42 S3 illustrates experimental quantitation of dissolved Fe²⁺ and calibration curve of Fe^{II}-
43 phenanthroline complexes; Figure S4 illustrate selected ion chromatograms (SIC`s) of Fe^{III}-citrate
44 complex ions; Figure S5 and S6 describe DI-HRMS screening and MS² experiments of Fe^{III}-citrate
45 complexes for identification and structural characterization. Figure S7 illustrates SIC`s for Fe^{III/II}-
46 citrate complexes detected in HPLC-HRMS. Figure S8 show *in situ* FlowCam Nano images of
47 colloidal particles. Figure S9 shows mass size distributions of colloids detected by FlowCam Nano.
48
49
50
51
52
53
54
55
56
57
58
59
60

1
2
3 Figure S10, S11 illustrate DI-HRMS results of dissolved colloidal products under specified
4 conditions. Figure S12 UV-visible spectrum of ferric oxalate photolysis. List of all molecular
5 assignments in HPLC-PDA-HRMS and DI-HRMS are reported in Table S1, S2, and S3.
6
7

8
9 **Data Availability** The dataset used for this work is available for download as a .zip file from
10 <https://doi.org/10.4231/xxx-yyyy> (West et al., 2022).
11
12
13

14 15 16 AUTHOR INFORMATION

17 18 **Corresponding Author**

19
20 **Alexander Laskin** – Department of Chemistry, Purdue University, Indiana 47906, United States;
21 orcid.org/0000-0002-7836-8417; Email: alaskin@purdue.edu
22
23

24 25 **Authors**

26
27 **Christopher P. West** – Department of Chemistry, Purdue University, Indiana 47906, United
28 States; orcid.org/0000-0001-9337-2820
29
30

31 **Jackson T. Ryan** – Department of Chemistry, Purdue University, Indiana 47906, United States
32

33 **Ana C. Morales** – Department of Chemistry, Purdue University, Indiana 47906, United States;
34 orcid.org/0000-0001-6969-2883
35
36

37 **Maria V. Misovich** – Department of Chemistry, Purdue University, Indiana 47906, United States;
38 orcid.org/0000-0001-6748-049X
39
40

41 **Anusha P. S. Hettiyadura** – Department of Chemistry, Purdue University, Indiana 47906, United
42 States; orcid.org/0000-0002-5757-9784
43
44

45 **Felipe Rivera-Adorno** – Department of Chemistry, Purdue University, Indiana 47906, United
46 States; orcid.org/0000-0002-7355-7999
47
48

49 **Jay M. Tomlin** – Department of Chemistry, Purdue University, Indiana 47906, United States;
50 orcid.org/0000-0002-3081-1512
51
52

53 **Andrew Darmody** – Department of Chemistry, Purdue University, Indiana 47906, United States;
54 orcid.org/0000-0002-7749-397X
55
56
57
58
59
60

1
2
3 **Brittany N. Linn** – Department of Chemistry, Purdue University, Indiana 47906, United States
4

5 **Peng Lin** – Department of Chemistry, Purdue University, Indiana 47906, United States
6
7
8
9

10 **Author Contributions.** C.P.W and A.L designed the overall project framework and experiments.
11 C.P.W, J.R, M.M, and B.N.L performed the photolysis and chemical actinometry experiments.
12 C.P.W, M.M, A.P.S.H, and P.L performed the LC separations and method development protocols.
13 C.P.W performed the molecular characterization experiments and processed, analyzed, and
14 interpreted the hyphenated LC-PDA-HRMS and direct infusion HRMS data with the assistance of
15 J.R, A.D., and B.N.L. F.R and J.M.T performed microscopy imaging. C.P.W and A.C.M
16 performed FlowCam measurements and data analysis. A.C.M designed custom MATLAB scripts
17 used for processing and analysis of all UV-visible spectroscopy data in this work. C.P.W and A.L
18 wrote the manuscript with contributions with all co-authors.
19
20
21
22
23
24
25
26
27
28

29 **Competing Interests.** The authors declare that they have no conflict of interest.
30
31
32
33

34 **Acknowledgments.** We acknowledge support from the startup funds allocated to A. Laskin by the
35 Department of Chemistry at Purdue University and partial support from the National Science
36 Foundation award AGS-2039985 at the time of this manuscript preparation.
37
38
39
40
41
42
43
44
45
46
47
48
49
50
51
52
53
54
55
56
57
58
59
60

REFERENCES

- (1) Huang, J.; Jones, A.; Waite, T. D.; Chen, Y.; Huang, X.; Rosso, K. M.; Kappler, A.; Mansor, M.; Tratnyek, P. G.; Zhang, H. Fe(II) Redox Chemistry in the Environment. *Chem. Rev.* **2021**.
- (2) Taylor, K. G.; Konhauser, K. O. Iron in Earth Surface Systems: A Major Player in Chemical and Biological Processes. *Elements* **2011**, *7* (2), 83–88.
- (3) Taylor, S. R. Abundance of Chemical Elements in the Continental Crust: A New Table. *Geochim. Cosmochim. Acta* **1964**, *28* (8), 1273–1285.
- (4) Hutchins, D. A.; Boyd, P. W. Marine Phytoplankton and the Changing Ocean Iron Cycle. *Nat. Clim. Change* **2016**, *6* (12), 1072–1079.
- (5) Lis, H.; Shaked, Y.; Kranzler, C.; Keren, N.; Morel, F. M. M. Iron Bioavailability to Phytoplankton: An Empirical Approach. *ISME J.* **2015**, *9* (4), 1003–1013.
- (6) Boyd, P. W.; Jickells, T.; Law, C. S.; Blain, S.; Boyle, E. A.; Buesseler, K. O.; Coale, K. H.; Cullen, J. J.; Baar, H. J. W. de; Follows, M.; Harvey, M.; Lancelot, C.; Levasseur, M.; Owens, N. P. J.; Pollard, R.; Rivkin, R. B.; Sarmiento, J.; Schoemann, V.; Smetacek, V.; Takeda, S.; Tsuda, A.; Turner, S.; Watson, A. J. Mesoscale Iron Enrichment Experiments 1993-2005: Synthesis and Future Directions. *Science* **2007**, *315* (5812), 612–617.
- (7) Jickells, T. D.; An, Z. S.; Andersen, K. K.; Baker, A. R.; Bergametti, G.; Brooks, N.; Cao, J. J.; Boyd, P. W.; Duce, R. A.; Hunter, K. A.; Kawahata, H.; Kubilay, N.; laRoche, J.; Liss, P. S.; Mahowald, N.; Prospero, J. M.; Ridgwell, A. J.; Tegen, I.; Torres, R. Global Iron Connections Between Desert Dust, Ocean Biogeochemistry, and Climate. *Science* **2005**, *308* (5718), 67–71.
- (8) Sedwick, P. N.; Sholkovitz, E. R.; Church, T. M. Impact of Anthropogenic Combustion Emissions on the Fractional Solubility of Aerosol Iron: Evidence from the Sargasso Sea. *Geochem. Geophys. Geosystems* **2007**, *8* (10).
- (9) Gonet, T.; Maher, B. A. Airborne, Vehicle-Derived Fe-Bearing Nanoparticles in the Urban Environment: A Review. *Environ. Sci. Technol.* **2019**, *53* (17), 9970–9991.
- (10) Deguillaume, L.; Leriche, M.; Desboeufs, K.; Mailhot, G.; George, C.; Chaumerliac, N. Transition Metals in Atmospheric Liquid Phases: Sources, Reactivity, and Sensitive Parameters. *Chem. Rev.* **2005**, *105* (9), 3388–3431.
- (11) Tomlin, J. M.; Jankowski, K. A.; Rivera-Adorno, F. A.; Fraund, M.; China, S.; Stirm, B. H.; Kaeser, R.; Eakins, G. S.; Moffet, R. C.; Shepson, P. B.; Laskin, A. Chemical Imaging of Fine Mode Atmospheric Particles Collected from a Research Aircraft over Agricultural Fields. *ACS Earth Space Chem.* **2020**, *4* (11), 2171–2184.
- (12) Cwiertny, D. M.; Baltrusaitis, J.; Hunter, G. J.; Laskin, A.; Scherer, M. M.; Grassian, V. H. Characterization and Acid-Mobilization Study of Iron-Containing Mineral Dust Source Materials. *J. Geophys. Res. Atmospheres* **2008**, *113* (D5).
- (13) Al-Abadleh, H. A. Aging of Atmospheric Aerosols and the Role of Iron in Catalyzing Brown Carbon Formation. *Environ. Sci. Atmospheres* **2021**, *1* (6), 297–345.
- (14) Tagliabue, A.; Bowie, A. R.; Boyd, P. W.; Buck, K. N.; Johnson, K. S.; Saito, M. A. The Integral Role of Iron in Ocean Biogeochemistry. *Nature* **2017**, *543* (7643), 51–59.
- (15) Kappler, A.; Bryce, C.; Mansor, M.; Lueder, U.; Byrne, J. M.; Swanner, E. D. An Evolving View on Biogeochemical Cycling of Iron. *Nat. Rev. Microbiol.* **2021**, *19* (6), 360–374.
- (16) Lovley, D. R.; Holmes, D. E.; Nevin, K. P. Dissimilatory Fe(III) and Mn(IV) Reduction. In *Advances in Microbial Physiology*; Academic Press, 2004; Vol. 49, pp 219–286.
- (17) Bosch, J.; Heister, K.; Hofmann, T.; Meckenstock, R. U. Nanosized Iron Oxide Colloids Strongly Enhance Microbial Iron Reduction. *Appl. Environ. Microbiol.* **2010**, *76* (1), 184–189.
- (18) Roden, E. E. Geochemical and Microbiological Controls on Dissimilatory Iron Reduction. *Comptes Rendus Geosci.* **2006**, *338* (6), 456–467.

- 1
2
3 (19) Lueder, U.; Barker Jørgensen, B.; Kappler, A.; Schmidt, C. Photochemistry of Iron in Aquatic
4 Environments. *Environ. Sci. Process. Impacts* **2020**, *22* (1), 12–24.
- 5 (20) Pozdnyakov, I. P.; Kolomeets, A. V.; Plyusnin, V. F.; Melnikov, A. A.; Kompanets, V. O.; Chekalin, S.
6 V.; Tkachenko, N.; Lemmetyinen, H. Photophysics of Fe(III)–Tartrate and Fe(III)–Citrate Complexes
7 in Aqueous Solutions. *Chem. Phys. Lett.* **2012**, *530*, 45–48.
- 8 (21) Vukosav, P.; Mlakar, M.; Tomišić, V. Revision of Iron(III)–Citrate Speciation in Aqueous Solution.
9 Voltammetric and Spectrophotometric Studies. *Anal. Chim. Acta* **2012**, *745*, 85–91.
- 10 (22) Weller, C.; Horn, S.; Herrmann, H. Photolysis of Fe(III) Carboxylate Complexes: Fe(II) Quantum
11 Yields and Reaction Mechanisms. *J. Photochem. Photobiol. Chem.* **2013**, *268*, 24–36.
- 12 (23) Pozdnyakov, I. P.; Melnikov, A. A.; Tkachenko, N.; Chekalin, S. V.; Lemmetyinen, H.; Plyusnin, V. F.
13 Ultrafast Photophysical Processes for Fe(III)-Carboxylates. *Dalton Trans.* **2014**, *43* (47), 17590–
14 17595.
- 15 (24) Glebov, E. M.; Pozdnyakov, I. P.; Grivin, V. P.; Plyusnin, V. F.; Zhang, X.; Wu, F.; Deng, N.
16 Intermediates in Photochemistry of Fe(III) Complexes with Carboxylic Acids in Aqueous Solutions.
17 *Photochem. Photobiol. Sci.* **2011**, *10* (3), 425–430.
- 18 (25) Abrahamson, H. B.; Rezvani, A. B.; Brushmiller, J. G. Photochemical and Spectroscopic Studies of
19 Complexes, of Iron(III) with Citric Acid and Other Carboxylic Acids. *Inorganica Chim. Acta* **1994**, *226*
20 (1), 117–127.
- 21 (26) Weller, C.; Tilgner, A.; Bräuer, P.; Herrmann, H. Modeling the Impact of Iron–Carboxylate
22 Photochemistry on Radical Budget and Carboxylate Degradation in Cloud Droplets and Particles.
23 *Environ. Sci. Technol.* **2014**, *48* (10), 5652–5659.
- 24 (27) George, C.; D’Anna, B.; Herrmann, H.; Weller, C.; Vaida, V.; Donaldson, D. J.; Bartels-Rausch, T.;
25 Ammann, M. Emerging Areas in Atmospheric Photochemistry. In *Atmospheric and Aerosol*
26 *Chemistry*; McNeill, V. F., Ariya, P. A., Eds.; Topics in Current Chemistry; Springer: Berlin,
27 Heidelberg, 2014; pp 1–53.
- 28 (28) Mangiante, David. M.; Schaller, R. D.; Zarzycki, P.; Banfield, J. F.; Gilbert, B. Mechanism of Ferric
29 Oxalate Photolysis. *ACS Earth Space Chem.* **2017**, *1* (5), 270–276.
- 30 (29) Borer, P.; Hug, S. J. Photo-Redox Reactions of Dicarboxylates and α -Hydroxydicarboxylates at the
31 Surface of Fe(III)(Hydr)Oxides Followed with in Situ ATR-FTIR Spectroscopy. *J. Colloid Interface Sci.*
32 **2014**, *416*, 44–53.
- 33 (30) Herrmann, H.; Schaefer, T.; Tilgner, A.; Styler, S. A.; Weller, C.; Teich, M.; Otto, T. Tropospheric
34 Aqueous-Phase Chemistry: Kinetics, Mechanisms, and Its Coupling to a Changing Gas Phase. *Chem.*
35 *Rev.* **2015**, *115* (10), 4259–4334.
- 36 (31) Wasgestian, F. V. Balzani Und V. Carassiti: Photochemistry of Coordination Compounds. Academic
37 Press, London, New York 1970. 432 Seiten. Preis: 150 s.; 1971.
- 38 (32) Cieśla, P.; Kocot, P.; Mytych, P.; Stasicka, Z. Homogeneous Photocatalysis by Transition Metal
39 Complexes in the Environment. *J. Mol. Catal. Chem.* **2004**, *224* (1), 17–33.
- 40 (33) Feng, W.; Nansheng, D.; Glebov, E. M.; Pozdnyakov, I. P.; Grivin, V. P.; Plyusnin, V. F.; Bazhin, N. M.
41 Kinetics and Mechanism of Photolysis of the Iron(III) Complex with Tartaric Acid. *Russ. Chem. Bull.*
42 **2007**, *56* (5), 900–903.
- 43 (34) Pozdnyakov, I. P.; Kel, O. V.; Plyusnin, V. F.; Grivin, V. P.; Bazhin, N. M. New Insight into
44 Photochemistry of Ferrioxalate. *J. Phys. Chem. A* **2008**, *112* (36), 8316–8322.
- 45 (35) Zhang, X.; Gong, Y.; Wu, F.; Deng, N.; Pozdnyakov, I. P.; Glebov, E. M.; Grivin, V. P.; Plyusnin, V. F.;
46 Bazhinb, N. M. Photochemistry of the Iron(III) Complex with Pyruvic Acid in Aqueous Solutions.
47 *Russ. Chem. Bull.* **2009**, *58* (9), 1828–1836.
- 48 (36) Abel, B.; Assmann, J.; Buback, M.; Grimm, C.; Kling, M.; Schmatz, S.; Schroeder, J.; Witte, T.
49 Ultrafast Decarboxylation of Carbonyloxy Radicals: Influence of Molecular Structure. *J. Phys.*
50 *Chem. A* **2003**, *107* (45), 9499–9510.
- 51
52
53
54
55
56
57
58
59
60

- 1
2
3 (37) Bockman, T. M.; Hubig, S. M.; Kochi, J. K. Direct Observation of Ultrafast Decarboxylation of
4 Acyloxy Radicals via Photoinduced Electron Transfer in Carboxylate Ion Pairs. *J. Org. Chem.* **1997**,
5 62 (7), 2210–2221.
- 6 (38) Hilborn, J. W.; Pincock, J. A. Rates of Decarboxylation of Acyloxy Radicals Formed in the
7 Photocleavage of Substituted 1-Naphthylmethyl Alkanoates. *J. Am. Chem. Soc.* **1991**, 113 (7),
8 2683–2686.
- 9 (39) Sonntag, C. von; Schuchmann, H.-P. The Elucidation of Peroxyl Radical Reactions in Aqueous
10 Solution with the Help of Radiation-Chemical Methods. *Angew. Chem. Int. Ed. Engl.* **1991**, 30 (10),
11 1229–1253.
- 12 (40) George, C.; Ammann, M.; D’Anna, B.; Donaldson, D. J.; Nizkorodov, S. A. Heterogeneous
13 Photochemistry in the Atmosphere. *Chem. Rev.* **2015**, 115 (10), 4218–4258.
- 14 (41) Dou, J.; Alpert, P. A.; Corral Arroyo, P.; Luo, B.; Schneider, F.; Xto, J.; Huthwelker, T.; Borca, C. N.;
15 Henzler, K. D.; Raabe, J.; Watts, B.; Herrmann, H.; Peter, T.; Ammann, M.; Krieger, U. K.
16 Photochemical Degradation of Iron(III) Citrate/Citric Acid Aerosol Quantified with the Combination
17 of Three Complementary Experimental Techniques and a Kinetic Process Model. *Atmospheric*
18 *Chem. Phys.* **2021**, 21 (1), 315–338.
- 19 (42) Zuo, Y.; Hoigne, J. Formation of Hydrogen Peroxide and Depletion of Oxalic Acid in Atmospheric
20 Water by Photolysis of Iron(III)-Oxalato Complexes. *Environ. Sci. Technol.* **1992**, 26 (5), 1014–1022.
- 21 (43) Zepp, R. G.; Faust, B. C.; Hoigne, J. Hydroxyl Radical Formation in Aqueous Reactions (PH 3-8) of
22 Iron(II) with Hydrogen Peroxide: The Photo-Fenton Reaction. *Environ. Sci. Technol.* **1992**, 26 (2),
23 313–319.
- 24 (44) Balmer, M. E.; Sulzberger, B. Atrazine Degradation in Irradiated Iron/Oxalate Systems: Effects of
25 PH and Oxalate. *Environ. Sci. Technol.* **1999**, 33 (14), 2418–2424.
- 26 (45) Southworth, B. A.; Voelker, B. M. Hydroxyl Radical Production via the Photo-Fenton Reaction in the
27 Presence of Fulvic Acid. *Environ. Sci. Technol.* **2003**, 37 (6), 1130–1136.
- 28 (46) Fenton, H. J. H. LXXIII.—Oxidation of Tartaric Acid in Presence of Iron. *J. Chem. Soc. Trans.* **1894**, 65
29 (0), 899–910.
- 30 (47) Zhang, C.; Wang, L.; Wu, F.; Deng, N. Quantitation of Hydroxyl Radicals from Photolysis of Fe(III)-
31 Citrate Complexes in Aerobic Water (5 Pp). *Environ. Sci. Pollut. Res.* **2006**, 13 (3), 156–160.
- 32 (48) Kim, S.-M.; Vogelpohl, A. Degradation of Organic Pollutants by the Photo-Fenton-Process. *Chem.*
33 *Eng. Technol.* **1998**, 21 (2), 187–191.
- 34 (49) Sun, Yunfu.; Pignatello, J. J. Activation of Hydrogen Peroxide by Iron(III) Chelates for Abiotic
35 Degradation of Herbicides and Insecticides in Water. *J. Agric. Food Chem.* **1993**, 41 (2), 308–312.
- 36 (50) Fukushima, M.; Tatsumi, K. Degradation Pathways of Pentachlorophenol by Photo-Fenton Systems
37 in the Presence of Iron(III), Humic Acid, and Hydrogen Peroxide. *Environ. Sci. Technol.* **2001**, 35 (9),
38 1771–1778.
- 39 (51) Marchetti, B.; Karsili, T. N. V.; Ashfold, M. N. R. Exploring Norrish Type I and Type II Reactions: An
40 Ab Initio Mechanistic Study Highlighting Singlet-State Mediated Chemistry. *Phys. Chem. Chem.*
41 *Phys.* **2019**, 21 (26), 14418–14428.
- 42 (52) Norrish, R. G. W.; Appleyard, M. E. S. 191. Primary Photochemical Reactions. Part IV.
43 Decomposition of Methyl Ethyl Ketone and Methyl Butyl Ketone. *J. Chem. Soc. Resumed* **1934**, No.
44 0, 874–880.
- 45 (53) Pitts, J. N.; Blacet, F. E. METHYL ETHYL KETONE PHOTOCHEMICAL PROCESSES. *J. Am. Chem. Soc.*
46 **1950**, 72 (6), 2810–2811.
- 47 (54) Norrish, R. G. W.; Bamford, C. H. Photo-Decomposition of Aldehydes and Ketones. *Nature* **1937**,
48 140 (3535), 195–196.
- 49 (55) Alpert, P. A.; Dou, J.; Corral Arroyo, P.; Schneider, F.; Xto, J.; Luo, B.; Peter, T.; Huthwelker, T.;
50 Borca, C. N.; Henzler, K. D.; Schaefer, T.; Herrmann, H.; Raabe, J.; Watts, B.; Krieger, U. K.;
51
52
53
54
55
56
57
58
59
60

- 1
2
3 Ammann, M. Photolytic Radical Persistence Due to Anoxia in Viscous Aerosol Particles. *Nat.*
4 *Commun.* **2021**, *12* (1), 1769.
- 5 (56) Zhang, Y.; Xie, H. Photomineralization and Photomethanification of Dissolved Organic Matter in
6 Saguenay River Surface Water. *Biogeosciences* **2015**, *12* (22), 6823–6836.
- 7 (57) Borduas-Dedekind, N.; Ossola, R.; David, R. O.; Boynton, L. S.; Weichlinger, V.; Kanji, Z. A.; McNeill,
8 K. Photomineralization Mechanism Changes the Ability of Dissolved Organic Matter to Activate
9 Cloud Droplets and to Nucleate Ice Crystals. *Atmospheric Chem. Phys.* **2019**, *19* (19), 12397–12412.
- 10 (58) Barbeau, K.; Moffett, J. W. Laboratory and Field Studies of Colloidal Iron Oxide Dissolution as
11 Mediated by Phagotrophy and Photolysis. *Limnol. Oceanogr.* **2000**, *45* (4), 827–835.
- 12 (59) Wells, M. L.; Mayer, L. M.; Donard, O. F. X.; de Souza Sierra, M. M.; Ackelson, S. G. The Photolysis
13 of Colloidal Iron in the Oceans. *Nature* **1991**, *353* (6341), 248–250.
- 14 (60) Chen, X.; Ye, X.; Chu, W.; Olk, D. C.; Cao, X.; Schmidt-Rohr, K.; Zhang, L.; Thompson, M. L.; Mao, J.;
15 Gao, H. Formation of Char-Like, Fused-Ring Aromatic Structures from a Nonpyrogenic Pathway
16 during Decomposition of Wheat Straw. *J. Agric. Food Chem.* **2020**, *68* (9), 2607–2614.
- 17 (61) Abida, O.; Kolar, M.; Jirkovsky, J.; Mailhot, G. Degradation of 4-Chlorophenol in Aqueous Solution
18 Photoinduced by Fe(III)–Citrate Complex. *Photochem. Photobiol. Sci.* **2012**, *11* (5), 794–802.
- 19 (62) Faust, B. C.; Zepp, R. G. Photochemistry of Aqueous Iron(III)-Polycarboxylate Complexes: Roles in
20 the Chemistry of Atmospheric and Surface Waters. *Environ. Sci. Technol.* **1993**, *27* (12), 2517–2522.
- 21 (63) Arroyo, P. C.; Malecha, K. T.; Ammann, M.; Nizkorodov, S. A. Influence of Humidity and Iron(III) on
22 Photodegradation of Atmospheric Secondary Organic Aerosol Particles. *Phys. Chem. Chem. Phys.*
23 **2018**, *20* (47), 30021–30031.
- 24 (64) Aiona, P. K.; Lee, H. J.; Leslie, R.; Lin, P.; Laskin, A.; Laskin, J.; Nizkorodov, S. A. Photochemistry of
25 Products of the Aqueous Reaction of Methylglyoxal with Ammonium Sulfate. *ACS Earth Space*
26 *Chem.* **2017**, *1* (8), 522–532.
- 27 (65) Fleming, L. T.; Lin, P.; Roberts, J. M.; Selimovic, V.; Yokelson, R.; Laskin, J.; Laskin, A.; Nizkorodov, S.
28 A. Molecular Composition and Photochemical Lifetimes of Brown Carbon Chromophores in
29 Biomass Burning Organic Aerosol. *Atmospheric Chem. Phys.* **2020**, *20* (2), 1105–1129.
- 30 (66) Lin, P.; Fleming, L. T.; Nizkorodov, S. A.; Laskin, J.; Laskin, A. Comprehensive Molecular
31 Characterization of Atmospheric Brown Carbon by High Resolution Mass Spectrometry with
32 Electrospray and Atmospheric Pressure Photoionization. *Anal. Chem.* **2018**, *90* (21), 12493–12502.
- 33 (67) Lavi, A.; Lin, P.; Bhaduri, B.; Carmieli, R.; Laskin, A.; Rudich, Y. Characterization of Light-Absorbing
34 Oligomers from Reactions of Phenolic Compounds and Fe(III). *ACS Earth Space Chem.* **2017**, *1* (10),
35 637–646.
- 36 (68) Budisulistiorini, S. H.; Riva, M.; Williams, M.; Chen, J.; Itoh, M.; Surratt, J. D.; Kuwata, M. Light-
37 Absorbing Brown Carbon Aerosol Constituents from Combustion of Indonesian Peat and Biomass.
38 *Environ. Sci. Technol.* **2017**, *51* (8), 4415–4423.
- 39 (69) Lin, Y.-H.; Budisulistiorini, S. H.; Chu, K.; Siejack, R. A.; Zhang, H.; Riva, M.; Zhang, Z.; Gold, A.;
40 Kautzman, K. E.; Surratt, J. D. Light-Absorbing Oligomer Formation in Secondary Organic Aerosol
41 from Reactive Uptake of Isoprene Epoxydiols. *Environ. Sci. Technol.* **2014**, *48* (20), 12012–12021.
- 42 (70) West, C. P.; Hettiyadura, A. P. S.; Darmody, A.; Mahamuni, G.; Davis, J.; Novosselov, I.; Laskin, A.
43 Molecular Composition and the Optical Properties of Brown Carbon Generated by the Ethane
44 Flame. *ACS Earth Space Chem.* **2020**, *4* (7), 1090–1103.
- 45 (71) Siemens, K.; Morales, A.; He, Q.; Li, C.; Hettiyadura, A. P. S.; Rudich, Y.; Laskin, A. Molecular
46 Analysis of Secondary Brown Carbon Produced from the Photooxidation of Naphthalene. *Environ.*
47 *Sci. Technol.* **2022**, *56* (6), 3340–3353.
- 48 (72) Lee, H. J. (Julie); Aiona, P. K.; Laskin, A.; Laskin, J.; Nizkorodov, S. A. Effect of Solar Radiation on the
49 Optical Properties and Molecular Composition of Laboratory Proxies of Atmospheric Brown
50 Carbon. *Environ. Sci. Technol.* **2014**, *48* (17), 10217–10226.
- 51
52
53
54
55
56
57
58
59
60

- 1
2
3
4 (73) Silva, A. M. N.; Kong, X.; Parkin, M. C.; Cammack, R.; Hider, R. C. Iron(III) Citrate Speciation in
5 Aqueous Solution. *Dalton Trans.* **2009**, No. 40, 8616.
- 6 (74) Gautier-Luneau, I.; Merle, C.; Phanon, D.; Lebrun, C.; Biaso, F.; Serratrice, G.; Pierre, J.-L. New
7 Trends in the Chemistry of Iron(III) Citrate Complexes: Correlations between X-Ray Structures and
8 Solution Species Probed by Electrospray Mass Spectrometry and Kinetics of Iron Uptake from
9 Citrate by Iron Chelators. *Chem. – Eur. J.* **2005**, *11* (7), 2207–2219.
- 10 (75) Lehóczki, T.; Józsa, É.; Ósz, K. Ferrioxalate Actinometry with Online Spectrophotometric Detection.
11 *J. Photochem. Photobiol. Chem.* **2013**, *251*, 63–68.
- 12 (76) Stucki, J. W. The Quantitative Assay of Minerals for Fe²⁺ and Fe³⁺ Using 1,10-Phenanthroline: II. A
13 Photochemical Method. *Soil Sci. Soc. Am. J.* **1981**, *45* (3), 638–641.
- 14 (77) Stucki, J. W.; Anderson, W. L. The Quantitative Assay of Minerals for Fe²⁺ and Fe³⁺ Using 1,10-
15 Phenanthroline: I. Sources of Variability. *Soil Sci. Soc. Am. J.* **1981**, *45* (3), 633–637.
- 16 (78) Greco, G.; Letzel, T. Main Interactions and Influences of the Chromatographic Parameters in HILIC
17 Separations. *J. Chromatogr. Sci.* **2013**, *51* (7), 684–693.
- 18 (79) Buszewski, B.; Noga, S. Hydrophilic Interaction Liquid Chromatography (HILIC)—a Powerful
19 Separation Technique. *Anal. Bioanal. Chem.* **2012**, *402* (1), 231–247.
- 20 (80) AlChoubassi, G.; Aszyk, J.; Pisarek, P.; Bierla, K.; Ouerdane, L.; Szpunar, J.; Lobinski, R. Advances in
21 Mass Spectrometry for Iron Speciation in Plants. *TrAC Trends Anal. Chem.* **2018**, *104*, 77–86.
- 22 (81) Spagou, K.; Tsoukali, H.; Raikos, N.; Gika, H.; Wilson, I. D.; Theodoridis, G. Hydrophilic Interaction
23 Chromatography Coupled to MS for Metabonomic/Metabolomic Studies. *J. Sep. Sci.* **2010**, *33* (6–
24 7), 716–727.
- 25 (82) Dell'mour, M.; Schenkeveld, W.; Oburger, E.; Fischer, L.; Kraemer, S.; Puschenreiter, M.;
26 Lämmerhofer, M.; Koellensperger, G.; Hann, S. Analysis of Iron-Phytosiderophore Complexes in
27 Soil Related Samples: LC-ESI-MS/MS versus CE-MS. *ELECTROPHORESIS* **2012**, *33* (4), 726–733.
- 28 (83) Tsednee, M.; Mak, Y.-W.; Chen, Y.-R.; Yeh, K.-C. A Sensitive LC-ESI-Q-TOF-MS Method Reveals
29 Novel Phytosiderophores and Phytosiderophore–Iron Complexes in Barley. *New Phytol.* **2012**, *195*
30 (4), 951–961.
- 31 (84) Rellán-Álvarez, R.; Giner-Martínez-Sierra, J.; Orduna, J.; Orera, I.; Rodríguez-Castrillón, J. Á.; García-
32 Alonso, J. I.; Abadía, J.; Álvarez-Fernández, A. Identification of a Tri-Iron(III), Tri-Citrate Complex in
33 the Xylem Sap of Iron-Deficient Tomato Resupplied with Iron: New Insights into Plant Iron Long-
34 Distance Transport. *Plant Cell Physiol.* **2010**, *51* (1), 91–102.
- 35 (85) Xuan, Y.; Scheuermann, E. B.; Meda, A. R.; Hayen, H.; von Wirén, N.; Weber, G. Separation and
36 Identification of Phytosiderophores and Their Metal Complexes in Plants by Zwitterionic
37 Hydrophilic Interaction Liquid Chromatography Coupled to Electrospray Ionization Mass
38 Spectrometry. *J. Chromatogr. A* **2006**, *1136* (1), 73–81.
- 39 (86) Pluskal, T.; Castillo, S.; Villar-Briones, A.; Orešič, M. MZmine 2: Modular Framework for Processing,
40 Visualizing, and Analyzing Mass Spectrometry-Based Molecular Profile Data. *BMC Bioinformatics*
41 **2010**, *11* (1), 395.
- 42 (87) Kuhl, C.; Tautenhahn, R.; Böttcher, C.; Larson, T. R.; Neumann, S. CAMERA: An Integrated Strategy
43 for Compound Spectra Extraction and Annotation of LC/MS Data Sets. *Anal. Chem.* **2012**, *84* (1),
44 283–289.
- 45 (88) Myers, O. D.; Sumner, S. J.; Li, S.; Barnes, S.; Du, X. One Step Forward for Reducing False Positive
46 and False Negative Compound Identifications from Mass Spectrometry Metabolomics Data: New
47 Algorithms for Constructing Extracted Ion Chromatograms and Detecting Chromatographic Peaks.
48 *Anal. Chem.* **2017**, *89* (17), 8696–8703.
- 49 (89) Jaitly, N.; Mayampurath, A.; Littlefield, K.; Adkins, J. N.; Anderson, G. A.; Smith, R. D. Decon2LS: An
50 Open-Source Software Package for Automated Processing and Visualization of High Resolution
51 Mass Spectrometry Data. *BMC Bioinformatics* **2009**, *10* (1), 87.
- 52
53
54
55
56
57
58
59
60

- 1
2
3
4 (90) Roach, P. J.; Laskin, J.; Laskin, A. Higher-Order Mass Defect Analysis for Mass Spectra of Complex
5 Organic Mixtures. *Anal. Chem.* **2011**, *83* (12), 4924–4929.
- 6 (91) Vetter, W. F. W. McLafferty, F. Turecek. Interpretation of Mass Spectra. Fourth Edition (1993).
7 University Science Books, Mill Valley, California. *Biol. Mass Spectrom.* **1994**, *23* (6), 379–379.
- 8 (92) Chen, Y.; Bond, T. C. Light Absorption by Organic Carbon from Wood Combustion. *Atmospheric*
9 *Chem. Phys.* **2010**, *10* (4), 1773–1787.
- 10 (93) Kirchstetter, T. W.; Novakov, T.; Hobbs, P. V. Evidence That the Spectral Dependence of Light
11 Absorption by Aerosols Is Affected by Organic Carbon. *J. Geophys. Res. Atmospheres* **2004**, *109*
12 (D21).
- 13 (94) Hettiyadura, A. P. S.; Laskin, A. Quantitative Analysis of Polycyclic Aromatic Hydrocarbons Using
14 High-Performance Liquid Chromatography-Photodiode Array-High-Resolution Mass Spectrometric
15 Detection Platform Coupled to Electrospray and Atmospheric Pressure Photoionization Sources. *J.*
16 *Mass Spectrom.* **2022**, *57* (2), e4804.
- 17 (95) Hettiyadura, A. P. S.; Garcia, V.; Li, C.; West, C. P.; Tomlin, J.; He, Q.; Rudich, Y.; Laskin, A. Chemical
18 Composition and Molecular-Specific Optical Properties of Atmospheric Brown Carbon Associated
19 with Biomass Burning. *Environ. Sci. Technol.* **2021**, *55* (4), 2511–2521.
- 20 (96) Krause, N.; Kuhn, S.; Frotscher, E.; Nikels, F.; Hawe, A.; Garidel, P.; Menzen, T. Oil-Immersion Flow
21 Imaging Microscopy for Quantification and Morphological Characterization of Submicron Particles
22 in Biopharmaceuticals. *AAPS J.* **2021**, *23* (1), 13.
- 23 (97) Hasberg, A. K. M.; Bijaksana, S.; Held, P.; Just, J.; Melles, M.; Morlock, M. A.; Opitz, S.; Russell, J. M.;
24 Vogel, H.; Wennrich, V. Modern Sedimentation Processes in Lake Towuti, Indonesia, Revealed by
25 the Composition of Surface Sediments. *Sedimentology* **2019**, *66* (2), 675–698.
- 26 (98) Seraghni, N.; Belattar, S.; Mameri, Y.; Debbache, N.; Sehili, T. Fe(III)-Citrate-Complex-Induced
27 Photooxidation of 3-Methylphenol in Aqueous Solution
28 <https://www.hindawi.com/journals/ijp/2012/630425/> (accessed 2021 -03 -02).
29 <https://doi.org/10.1155/2012/630425>.
- 30 (99) Ruales-Lonfat, C.; Barona, J. F.; Sienkiewicz, A.; Vélez, J.; Benítez, L. N.; Pulgarín, C. Bacterial
31 Inactivation with Iron Citrate Complex: A New Source of Dissolved Iron in Solar Photo-Fenton
32 Process at near-Neutral and Alkaline PH. *Appl. Catal. B Environ.* **2016**, *180*, 379–390.
- 33 (100) Ogi, Y.; Obara, Y.; Katayama, T.; Suzuki, Y.-I.; Liu, S. Y.; Bartlett, N. C.-M.; Kurahashi, N.;
34 Karashima, S.; Togashi, T.; Inubushi, Y.; Ogawa, K.; Owada, S.; Rubešová, M.; Yabashi, M.; Misawa,
35 K.; Slaviček, P.; Suzuki, T. Ultraviolet Photochemical Reaction of [Fe(III)(C₂O₄)₃]³⁻ in Aqueous
36 Solutions Studied by Femtosecond Time-Resolved X-Ray Absorption Spectroscopy Using an X-Ray
37 Free Electron Laser. *Struct. Dyn.* **2015**, *2* (3), 034901.
- 38 (101) Dekkiche, B. A.; Seraghni, N.; Debbache, N.; Ghoul, I.; Sehili, T. Effect of Natural and Artificial
39 Light on Fe(III) Organic Complexes Photolysis: Case of Fe (III)-Malonate and Fe(III)-Malate. *Int. J.*
40 *Chem. React. Eng.* **2019**, *17* (2).
- 41 (102) Wang, L.; Zhang, C.; Mestankova, H.; Wu, F.; Deng, N.; Pan, G.; Bolte, M.; Mailhot, G.
42 Photoinduced Degradation of 2,4-Dichlorophenol in Water: Influence of Various Fe(III)
43 Carboxylates. *Photochem. Photobiol. Sci.* **2009**, *8* (7), 1059–1065.
- 44 (103) Fu, Z.; Chen, R. Study of Complexes of Tannic Acid with Fe(III) and Fe(II). *J. Anal. Methods Chem.*
45 **2019**, *2019*, e3894571.
- 46 (104) Thorarinsdottir, A. E.; Gaudette, A. I.; Harris, T. D. Spin-Crossover and High-Spin Iron(II)
47 Complexes as Chemical Shift 19F Magnetic Resonance Thermometers. *Chem. Sci.* **2017**, *8* (3),
48 2448–2456.
- 49 (105) Baxendale, J. H.; Magee, J. The Photochemical Oxidation of Benzene in Aqueous Solution by
50 Ferric Ion. *Trans. Faraday Soc.* **1955**, *51* (0), 205–213.
- 51
52
53
54
55
56
57
58
59
60

- 1
2
3
4 (106) Moffett, J. W.; Zika, R. G. Reaction Kinetics of Hydrogen Peroxide with Copper and Iron in
5 Seawater. *Environ. Sci. Technol.* **1987**, *21* (8), 804–810.
- 6 (107) Quici, N.; Morgada, M. E.; Gettar, R. T.; Bolte, M.; Litter, M. I. Photocatalytic Degradation of
7 Citric Acid under Different Conditions: TiO₂ Heterogeneous Photocatalysis against Homogeneous
8 Photolytic Processes Promoted by Fe(III) and H₂O₂. *Appl. Catal. B Environ.* **2007**, *71* (3), 117–124.
- 9 (108) Waite, T. D.; Morel, F. M. Photoreductive Dissolution of Colloidal Iron Oxides in Natural Waters.
10 *Environ. Sci. Technol.* **1984**, *18* (11), 860–868.
- 11 (109) Meng, X.; Ryu, J.; Kim, B.; Ko, S. Application of Iron Oxide as a PH-Dependent Indicator for
12 Improving the Nutritional Quality. *Clin. Nutr. Res.* **2016**, *5* (3), 172–179.
- 13 (110) Li, F.; Koopal, L.; Tan, W. Roles of Different Types of Oxalate Surface Complexes in Dissolution
14 Process of Ferrihydrite Aggregates. *Sci. Rep.* **2018**, *8* (1), 2060.
- 15 (111) Borer, P.; Hug, S. J.; Sulzberger, B.; Kraemer, S. M.; Kretzschmar, R. Photolysis of Citrate on the
16 Surface of Lepidocrocite: An in Situ Attenuated Total Reflection Infrared Spectroscopy Study. *J.*
17 *Phys. Chem. C* **2007**, *111* (28), 10560–10569.
- 18 (112) Lv, Y.; Liu, J.; Zhu, R.; Zhu, J.; Chen, Q.; Liang, X.; He, H. Photoreductive Dissolution of Iron
19 (Hydr)Oxides and Its Geochemical Significance. *ACS Earth Space Chem.* **2022**.
- 20 (113) Silva, A. M. N.; Kong, X.; Parkin, M. C.; Cammack, R.; Hider, R. C. Iron(III) Citrate Speciation in
21 Aqueous Solution. *Dalton Trans.* **2009**, No. 40, 8616–8625.
- 22 (114) National Center for Biotechnology Information. “PubChem Compound Summary for CID
23 14298643, Ferrous Citrate” PubChem, Accessed 18 December, 2020.
- 24 (115) Pierre, J. L.; Gautier-Luneau, I. Iron and Citric Acid: A Fuzzy Chemistry of Ubiquitous Biological
25 Relevance. *Biometals* **2000**, *13* (1), 91–96.
- 26 (116) Königsberger, L.-C.; Königsberger, E.; May, P. M.; Hefter, G. T. Complexation of Iron(III) and
27 Iron(II) by Citrate. Implications for Iron Speciation in Blood Plasma. *J. Inorg. Biochem.* **2000**, *78* (3),
28 175–184.
- 29 (117) Pham, A. N.; Waite, T. D. Oxygenation of Fe(II) in the Presence of Citrate in Aqueous Solutions at
30 PH 6.0–8.0 and 25 °C: Interpretation from an Fe(II)/Citrate Speciation Perspective. *J. Phys. Chem. A*
31 **2008**, *112* (4), 643–651.
- 32 (118) Harris, D. C.; Aisen, P. Facilitation of Fe(II) Antioxidation by Fe(III) Complexing Agents. *Biochim.*
33 *Biophys. Acta BBA - Gen. Subj.* **1973**, *329* (1), 156–158.
- 34 (119) Liu, M. J.; Wiegel, A. A.; Wilson, K. R.; Houle, F. A. Aerosol Fragmentation Driven by Coupling of
35 Acid–Base and Free-Radical Chemistry in the Heterogeneous Oxidation of Aqueous Citric Acid by
36 OH Radicals. *J. Phys. Chem. A* **2017**, *121* (31), 5856–5870.
- 37 (120) Moharreh-Khiabani, D.; Linker, R. A.; Gold, R.; Stangel, M. Fumaric Acid and Its Esters: An
38 Emerging Treatment for Multiple Sclerosis. *Curr. Neuropharmacol.* **2009**, *7* (1), 60–64.
- 39 (121) Poncek, M.; Hayeck, N.; Emmelin, C.; George, C. Heterogeneous Photochemistry of Dicarboxylic
40 Acids on Mineral Dust. *Atmos. Environ.* **2019**, *212*, 262–271.
- 41 (122) Mazurek, A.; Jamroz, J. Precision of Dehydroascorbic Acid Quantitation with the Use of the
42 Subtraction Method – Validation of HPLC–DAD Method for Determination of Total Vitamin C in
43 Food. *Food Chem.* **2015**, *173*, 543–550.
- 44 (123) Dewhirst, R. A.; Fry, S. C. The Oxidation of Dehydroascorbic Acid and 2,3-Diketogulonate by
45 Distinct Reactive Oxygen Species. *Biochem. J.* **2018**, *475* (21), 3451–3470.
- 46 (124) Siegmann, K.; Sattler, K. Formation Mechanism for Polycyclic Aromatic Hydrocarbons in
47 Methane Flames. *J. Chem. Phys.* **2000**, *112* (2), 698–709.
- 48 (125) Cain, J.; Laskin, A.; Kholghy, M. R.; Thomson, M. J.; Wang, H. Molecular Characterization of
49 Organic Content of Soot along the Centerline of a Coflow Diffusion Flame. *Phys. Chem. Chem. Phys.*
50 **2014**, *16* (47), 25862–25875.
- 51
52
53
54
55
56
57
58
59
60

- 1
2
3 (126) Saleh, R. From Measurements to Models: Toward Accurate Representation of Brown Carbon in
4 Climate Calculations. *Curr. Pollut. Rep.* **2020**, *6* (2), 90–104.
- 5 (127) Zhou, Y.; West, C. P.; Hettiyadura, A. P. S.; Niu, X.; Wen, H.; Cui, J.; Shi, T.; Pu, W.; Wang, X.;
6 Laskin, A. Measurement Report: Molecular Composition, Optical Properties, and Radiative Effects
7 of Water-Soluble Organic Carbon in Snowpack Samples from Northern Xinjiang, China.
8 *Atmospheric Chem. Phys.* **2021**, *21* (11), 8531–8555.
- 9 (128) Alexander, D. T. L.; Crozier, P. A.; Anderson, J. R. Brown Carbon Spheres in East Asian Outflow
10 and Their Optical Properties. *Science* **2008**, *321* (5890), 833–836.
- 11 (129) Misovich, M. V.; Hettiyadura, A. P. S.; Jiang, W.; Zhang, Q.; Laskin, A. Molecular-Level Study of
12 the Photo-Oxidation of Aqueous-Phase Guaiacyl Acetone in the Presence of 3C*: Formation of
13 Brown Carbon Products. *ACS Earth Space Chem.* **2021**, *5* (8), 1983–1996.
- 14 (130) Zangmeister, C. D.; You, R.; Lunny, E. M.; Jacobson, A. E.; Okumura, M.; Zachariah, M. R.;
15 Radney, J. G. Measured In-Situ Mass Absorption Spectra for Nine Forms of Highly-Absorbing
16 Carbonaceous Aerosol. *Carbon* **2018**, *136*, 85–93.
- 17 (131) Miles, C. J.; Brezonik, P. L. Oxygen Consumption in Humic-Colored Waters by a Photochemical
18 Ferrous-Ferric Catalytic Cycle. *Environ. Sci. Technol.* **1981**, *15* (9), 1089–1095.
- 19 (132) Byrne, J. M.; Klueglein, N.; Pearce, C.; Rosso, K. M.; Appel, E.; Kappler, A. Redox Cycling of Fe(II)
20 and Fe(III) in Magnetite by Fe-Metabolizing Bacteria. *Science* **2015**, *347* (6229), 1473–1476.
- 21 (133) Emmenegger, L.; Schönenberger, R.; Sigg, L.; Sulzberger, B. Light-Induced Redox Cycling of Iron
22 in Circumneutral Lakes. *Limnol. Oceanogr.* **2001**, *46* (1), 49–61.
- 23 (134) Cwiertny, D. M.; Young, M. A.; Grassian, V. H. Chemistry and Photochemistry of Mineral Dust
24 Aerosol. *Annu. Rev. Phys. Chem.* **2008**, *59* (1), 27–51.
- 25 (135) Siefert, R. L.; Pehkonen, S. O.; Erel, Y.; Hoffmann, M. R. Iron Photochemistry of Aqueous
26 Suspensions of Ambient Aerosol with Added Organic Acids. *Geochim. Cosmochim. Acta* **1994**, *58*
27 (15), 3271–3279.
- 28 (136) Pu, W.; Wang, X.; Wei, H.; Zhou, Y.; Shi, J.; Hu, Z.; Jin, H.; Chen, Q. Properties of Black Carbon and
29 Other Insoluble Light-Absorbing Particles in Seasonal Snow of Northwestern China. *The Cryosphere*
30 **2017**, *11* (3), 1213–1233.
- 31 (137) Shi, T.; Cui, J.; Chen, Y.; Zhou, Y.; Pu, W.; Xu, X.; Chen, Q.; Zhang, X.; Wang, X. Enhanced Light
32 Absorption and Reduced Snow Albedo Due to Internally Mixed Mineral Dust in Grains of Snow.
33 *Atmospheric Chem. Phys.* **2021**, *21* (8), 6035–6051.
- 34 (138) Zhou, Y.; West, C. P.; Hettiyadura, A. P. S.; Pu, W.; Shi, T.; Niu, X.; Wen, H.; Cui, J.; Wang, X.;
35 Laskin, A. Molecular Characterization of Water-Soluble Brown Carbon Chromophores in Snowpack
36 from Northern Xinjiang, China. *Environ. Sci. Technol.* **2022**, *56* (7), 4173–4186.
- 37
38
39
40
41
42
43
44
45
46
47
48
49
50
51
52
53
54
55
56
57
58
59
60